INVITED PAPER

Room-Temperature Selective-Metallization Processes Applied to 3-D-Printed and Flexible Materials for Wireless Sensing

This article describes sensors and radio-frequency (RF) components fabricated by using emerging additive manufacturing technologies (3-D printing, metal foil tape, liquid metal filling, electro and electroless plating, and surface embossing).

By Valentina Palazzi, *Senior Member IEEE*, Federico Alimenti, *Senior Member IEEE*, Leonardo Pierantozzi, Matteo Ribeca, Leonardo Balocchi, *Student Member IEEE*, Luca Valentini, Silvia Bittolo Bon, Paolo Mezzanotte, *Member IEEE*, Manos M. Tentzeris, *Fellow IEEE*, and Luca Roselli, *Fellow IEEE*

ABSTRACT | This article describes sensors and radio frequency (RF) components manufactured by applying selective-metallization processes (metal foil tape, liquid metal filling, electro and electroless plating, and surface embossing) to 3-D-printed and flexible dielectric substrates. All these technologies can be implemented at room temperature, thus enabling the adoption of unconventional materials and biopolymers with low glass transition temperatures. In this article, we also describe how the above technologies are used to manufacture wireless transponders for tracking and sensing applications. Several examples of RF components are reported, including antennas, beamforming networks, Doppler radars, and wireless passive transponders based on backscatter radio. Innovative circuit design approaches (such as the via-less approach) are presented and their impact on circuit manufacturing and recyclability is discussed.

KEYWORDS | 3-D printing; additive manufacturing; backscatter radio; bioplastics; cardboard; copper foil tape; embossed-surface patterning; eutectic alloy; fused deposition modeling (FDM); harmonic radar; harmonic transponder; liquid metal; metal foil tape; paper; room-temperature metallization; stereolithography (SLA); thermoplastics; wireless sensing.

Received 13 May 2024; revised 4 October 2024; accepted 10 October 2024. Date of current version 13 November 2024. This work was supported in part by the the Italian Ministry of University and Research (MUR), in the frame of the "PON 2022 Ricerca e Innovazione" action. This work was also supported in part by the Electronics Components and Systems for European Leadership (ECSEL) Joint Undertaking (JU) under Grant 876362, in part by the European Union's Horizon 2020 Research and Innovation Program, and in part by Finland, Austria, Belgium, Czechia, Germany, Italy, Latvia, Netherlands, Poland, Switzerland. This work received funding from the European Union - Next-GenerationEU - National Recovery and Resilience Plan (NRRP) – Mission 4 Component 2, investiment n. 1.1, Prin 2022 – Prometheus "4D printing self-deploying bio-enabled polymer scaffolds for the non-invasive treatment of bleeding intestinal ulcers", grant: 2022BZLTTK, CUP I53D23002200006. *(Corresponding author: Valentina Palazzi.)*

Valentina Palazzi, **Federico Alimenti**, **Leonardo Pierantozzi**, **Matteo Ribeca**, **Leonardo Balocchi**, **Paolo Mezzanotte**, and **Luca Roselli** are with the Department of Engineering, University of Perugia, 06125 Perugia, Italy (e-mail: valentina.palazzi@unipg.it).

Luca Valentini is with the Civil and Environmental Engineering Department, University of Perugia, 05100 Terni, Italy.

Silvia Bittolo Bon is with the Department of Physics and Geology, University of Perugia, 06123 Perugia, Italy.

Manos M. Tentzeris is with the School of Electrical and Computer Engineering, Georgia Institute of Technology, Atlanta, GA 30339 USA.

Digital Object Identifier 10.1109/JPROC.2024.3481315

I. INTRODUCTION

The implementation of emerging concepts, such as the Internet of Things (IoT) and digital twins, calls for

the introduction of a massive amount of electronics on everyday objects [1], [2]. Electronic systems can be used to collect data on the item status and to transmit this information wirelessly to a processing unit for subsequent elaboration, which makes sensors and radio frequency (RF) front ends the key components of IoT nodes [3], [4].

Due to the large number of IoT nodes envisioned in diverse IoT applications, keeping track of all the devices and providing periodic maintenance to them can be challenging or even impossible. Devices can be placed in remote areas or can be moving, which is the case of IoT nodes for supply chain monitoring. Therefore, first, designers need to guarantee the energy autonomy of the IoT nodes, to avoid periodic battery replacements [5], [6], [7]. In addition, they must replace traditional polluting materials used for electronics with green materials, to avoid causing a further increase both in pollution and in the generation of e-waste [8], [9].

Another important feature of electronics for the IoT is its conformability [10]. IoT devices must become part of the design of the hosting object, in order not to compromise its original aim and functionality. To this purpose, flexible materials or custom 3-D shapes are preferable to standard rigid printed circuit boards (PCBs).

Alternative manufacturing technologies, including additive manufacturing, can play a pivotal role in enabling IoT applications [11]. First, they help reduce the waste caused by the electronics production. Second, they allow us to use alternative materials, not purposely developed for electronics, which ease the integration of electronics with items and reduce their environmental footprint.

However, emerging processes must overcome several challenges. RF transmission lines, transducers, and printed circuits in general require both metallic and dielectric parts. To replace PCBs, we need to selectively deposit conductive materials on dielectric surfaces. Other transmission line structures, such as substrate-integrated waveguides and coaxial cables, require vias and metal coating. Generally, high-resolution metallic patterns are obtained using photolithography. However, some materials, such as paper and cardboard, are porous and cannot sustain the chemical bath in acid chloride or the photoresist developer.

Alternatively, ink-jet printing and screen printing have been thoroughly investigated [12]. These processes make it possible to deposit nanoparticle inks, such as silver ink, on different surfaces [13], [14], [15]. However, they have some drawbacks: nanoparticles are generally dispersed in solvents, which must be made evaporate using high-temperature curing steps [16], [17], [18]. These temperatures (generally well above 100 °C) are not sustainable for green materials, such as bioplastics, or other resins. Alternative strategies based on laser and UltraViolet (UV) curing have been investigated [19], [20], [21], [22], [23], [24]. However, such processes are energy consuming, are characterized by high cost and low yield, and can be incompatible with the massive tagging of low-cost items.

On the other hand, the adoption of alternative materials and processes can open the door to new functionalities. Fragile materials can be used as crack sensors, and flexible and bendable materials can be used as mechanical sensors [25], [26].

Three-dimensional printing can enable compact and lightweight structures in a variety of different applications. The 3-D-printed metallic waveguide and reflective components, including plasmonic waveguides, polarizers, and reflectarray antennas, as well as all-dielectric low-propagation loss hollow-core microstructured waveguides and fibers, and gradient-refracting index lenses, have been demonstrated up to terahertz (THz) frequencies [27], [28], [29]. The 3-D printing has been also used to create periodic microstructures to develop metamaterials with exotic electromagnetic, acoustic, thermal, and optical properties [30], [31], and mechanically tunable components (i.e., 4-D printing) [32]. However, very few selective-metallization techniques are reported at such frequencies, which require a number of different manufacturing processes. For instance, in [33], a 2-D array of gold helix structures is manufactured by combining multiphoton polymerization with spin coating, 3-D direct laser writing, and electrochemical gold deposition. Attempts to combine 3-D printing with nanotechnologies to manufactured 3-D-printed tissue engineering scaffolds have been reported as well [34].

In the design of RF wireless transponders and sensors, the flexibility of 3-D printing technologies can be leveraged to enhance the telecommunication capabilities of the nodes or enable microfluidics. This, combined with the adoption of low-power communication strategies based on backscatter radios or harmonic radar, can enable passive and green nodes for IoT applications.

In this article, emerging selective-metallization technologies at room temperature, which are therefore compatible with bioplastics and other materials characterized by low glass transition temperatures, are explored. Wireless sensing solutions developed leveraging the mechanical and chemical properties of the alternative materials used for electronics are showcased and their features are discussed.

This article is organized as follows. Section II is dedicated to the selective-metallization processes. The processes are described step by step and their main features are reported and compared with the other technologies. In Section III, antennas and feed networks manufactured with the reported processes are analyzed, while Section IV describes complete wireless transponders for sensing and tracking, highlighting their performance and potential in terms of integration with everyday objects and their recyclability.

II. ROOM-TEMPERATURE SELECTIVE-METALLIZATION TECHNIQUES

In this section, we will examine some of the most promising techniques to perform selective metallization

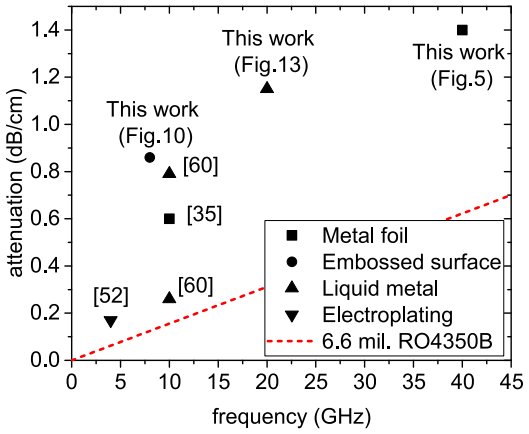

Fig. 1. ***Room-temperature selective-metallization techniques on unconventional materials and biopolymer for RF applications: attenuation per unit length of transmission lines manufactured with the reported processes versus operating frequency.***

on unconventional materials at room temperature for RF applications. The different techniques are characterized by variable complexity and features, leading to different pattern resolutions, surface roughness, and conductivity. The main features of these technologies are shown in Table 1. The "metal thickness" reported for liquid metal corresponds to the diameter of the channel in the scaffolding in which the liquid metal is pumped. The "skin depth" is calculated with the following equation:

$$\delta = \sqrt{\frac{2}{\omega\mu\sigma}} \tag{1}$$

where ω is the angular frequency, μ is the permeability of the metal, and σ is the conductivity of the metal. "RMS rough." stands for "root-mean-square surface roughness" (Sq). The minimum linewidth of the reported technologies is compatible with RF circuits in some cases up to millimeter-wave frequencies.

The measured attenuation per unit length versus frequency of transmission lines manufactured with the reported processes is shown in Fig. 1. All the reported values refer to microstrip lines except for the liquid metal, where coaxial lines are considered. The attenuation of a microstrip line implemented on a 6.6-mil RO4350B substrate is shown to compare the performance of the proposed emerging manufacturing technologies with standard RF PCBs.

These techniques are described in detail in the following.

A. Metal Foil Tape

The metal foil tape technique makes it possible to manufacture high-conductivity high-resolution metal patterns on different surfaces at room temperature. In the reported cases, this technique is applied to copper foil. The main process steps are shown in Fig. 2.

Copper foil tape generally consists of three layers: the copper layer, the glue layer, and the plastic protective layer. Standard photolithography steps can be applied to the copper tape exactly as they are applied to standard PCBs; a photoresist layer is deposited on top of the copper layer; a mask is placed between the photoresist and a UV lamp so that only the desired pattern is exposed to UV light. The exposed areas become soluble or insoluble depending on whether a positive or a negative photoresist is used. The areas corresponding to soluble photoresist are developed using dilute sodium [see Fig. 2(a)]. Then, the exposed copper is removed with a bath in acid chloride, as shown in Fig. 2(b); finally, the remaining photoresist is removed with a saturated sodium solution. A sacrificial layer is then applied to the top of the copper pattern and the protective layer beneath is removed, as shown in Fig. 2(c). The sacrificial layer (usually paper tape) is needed to avoid deformations in the metallic pattern during the protection removal and the transfer of the metal pattern to the substrate. Then, the copper tape is attached to the desired substrate [see Fig. 2(d)], and the sacrificial layer is peeled off [see Fig. 2(e)]. This way, all the metal patterns of one layer can be stuck in one step (even in the case of separated metal parts). If needed, a metal pattern can be applied on the top and the bottom of the given substrate, so as to obtain a double-layer circuit, as shown in Fig. 2(f) [36]. Alignment marks, such as holes or cuts, must be made to ensure proper alignment between the top and the bottom layers. In large-scale production, automated machines can be used to guarantee proper alignment, such as in PCB manufacturing. In principle, photolithography can be replaced by alternative techniques, such as laser cutting or stamping, and this technique can be applied to foils of different materials, such as aluminum.

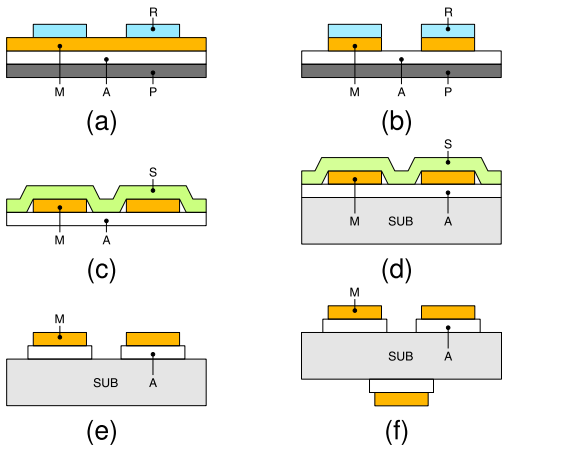

Fig. 2. ***Copper foil tape technology: process steps for the circuit fabrication. M: metal, A: adhesive, P: protection, R: photoresist, S: sacrificial layer, and SUB: hosting substrate. After [35]. (a) Copper foil with photoresist pattern, (b) copper foil after chemical etching with ferric chloride, (c) application of the sacrificial layer on top of the obtained copper pattern and removal of the protection layer underneath the copper foil, (d) application of the copper pattern to the hosting substrate, (e) removal of the sacrificial layer, and (f) in case of double layer circuits, application of a second copper pattern on the other side of the substrate.***

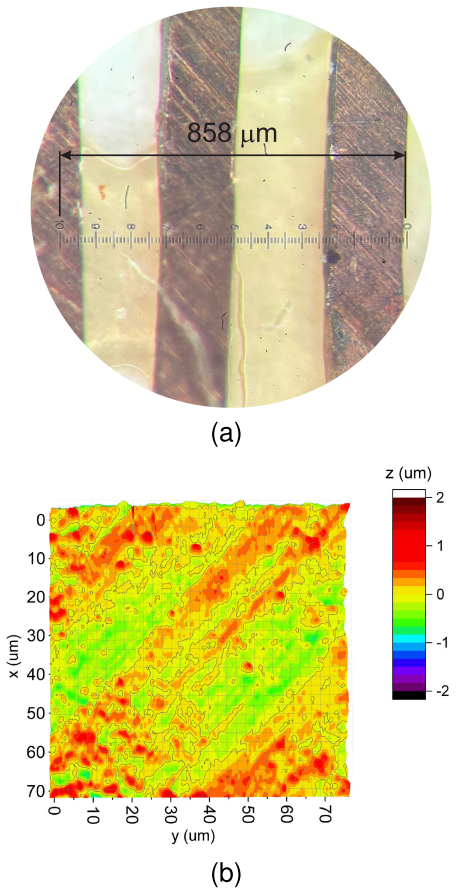

Fig. 3. *Details of the metal patterns manufactured with the copper foil tape process. (a) Optical image. (b) Atomic force microscope image. Each division of the optical image corresponds to 8.58 μm. Sa = 207 nm and Sq = 263 nm.*

The described metal foil tape technique can be defined as "semi-additive" since the process applied to copper is subtractive, but once the pattern is ready, it is "added" to the surface of the prototype. This way, the dielectric substrate is not subject to photolithography steps, and even porous and fragile materials, such as paper and cardboard, can be adopted.

Fig. 3 shows a few details of the deposited metal patterns. The minimum linewidth manufactured with this technique is 200 μm (measured value: 197.34 μm). The measured average surface roughness Sa is 207 nm, while the root-mean-square roughness (i.e., standard deviation) Sq is 263 nm. The surface roughness depends on the surface features of the copper foil and on how copper is applied to the substrate.

It is worth mentioning that the dielectric substrate obtained using this approach is not homogeneous, as two thin glue layers are interposed between each metal layer and the proper substrate, as shown in the insert of Fig. 4(a). To extract the electromagnetic parameters of the homogeneous equivalent substrate, resonant structures manufactured with the copper tape technique have been used. The S-parameters of the structures are then measured and compared with full-wave simulations where the same metal pattern is applied to an equivalent substrate (thickness of the equivalent substrate equal to the sum of the actual substrate plus the two glue layers). The permittivity and loss tangent of the equivalent substrate are varied until a good agreement between simulations and measurements is achieved.

This technique has several advantages. First, metal patterns can be applied to a broad variety of materials at room temperature. The traces have a bulk conductivity, meaning that high-quality resonators can be manufactured with this technique. Since the metal trace is a solid layer, lumped components can be soldered using standard soldering pastes. Finally, the dielectric acrylic glue below the copper layer can be used to manufacture overpass and parallel-plate capacitors, as demonstrated in [38].

Fig. 4(a) shows a microstrip T-resonator on a paper substrate, where the metal pattern is manufactured using copper foil. The S-parameters of the resonators are shown in Fig. 4(b). The circuit resonates at 23.5 GHz. Despite the high loss tangent of the paper substrate (about 0.08), an unloaded quality factor of 32 is obtained.

Finally, a 50-Ω microstrip line is manufactured on a slab of Poly(3-hydroxybutyrate-co-3-hydroxyvalerate) (PHBV) substrate. PHBV is a biopolymer that is typically obtained through a fermentation process that uses, as feedstock, sugar beets or canes agrowastes, and it is highly biodegradable and bioresorbable [40]. Fig. 5(a) shows a photograph of the line prototype, while Fig. 5(b) shows the measured S-parameters. The transmission coefficient is equal to -2.8 dB at 40 GHz, corresponding to an attenuation of 0.14 dB/mm.

B. Embossed-Surface Patterning

This technique, first described in [41], can be used for laboratory validation to create metal patterns on 3-D-printed surfaces. The main process steps are shown in Fig. 6. According to this approach, the areas of the 3-D-printed dielectric scaffolding that must be metalized are extruded in a protruded fashion with respect to the

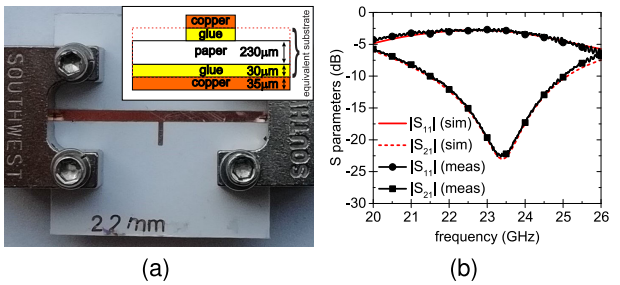

Fig. 4. *Microstrip T-resonator manufactured using copper foil tape on paper. (a) Prototype with insert on substrate cross section. (b) S-parameters. The feed line has a length of 2 cm (1 cm for each side) and a width of 1 mm. The width of the stub amounts to 0.4 mm, and its length is 2.2 mm. "sim" stands for simulation and "meas" for measurement. After [37].*

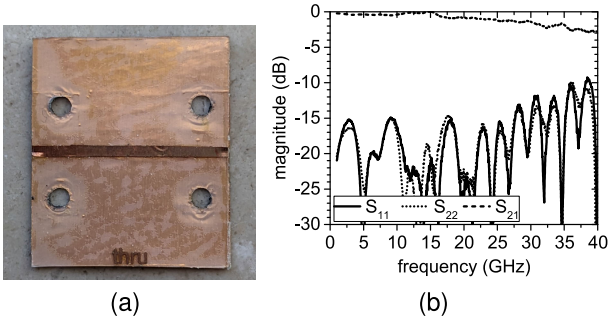

Fig. 5. *Microstrip line manufactured on PHBV with the metal foil process. (a) Photograph of the prototype. (b) Measured S-parameters from 1 to 40 GHz. Main parameters of the prototype—thickness: 360 μm, permittivity 2.95 at 35 GHz, loss tangent 0.015 at 35 GHz, line length: 2 cm, and linewidth: 1 mm [39].*

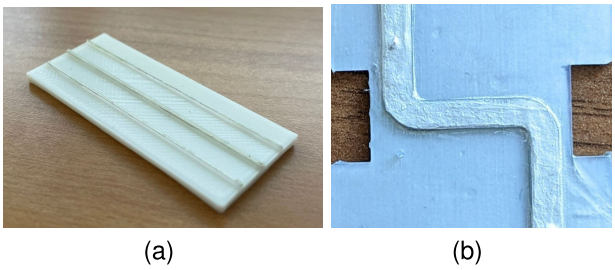

Fig. 7. *Microstrip lines manufactured with the 3-D printing-based embossed-surface patterning process. (a) Photograph of the prototype on PLA (FDM). (b) Photograph of the prototype on the Clear resin (SLA).*

rest of the surface [the step height is indicated with "h_1" and "h_2" in Fig. 6(a)]. For this purpose, microstrip lines are embossed with respect to the rest of the surface, while slots are engraved. Metallization is carried out by applying colloidal silver paste to the embossed areas with a brush, as shown in Fig. 6(b). Fig. 6(c) shows the dielectric with the embossed metalized patterns. Similar effects can be achieved by using a multijet printing tool, able to deposit both conductive and dielectric material [42], or using fused deposition modeling (FDM) printers with multiple extruders [43], although the reported conductivity and resolution of extruded conductive material is still generally low for RF applications [44].

Fig. 7 shows 3-D-printed lines with different widths. In Fig. 7(a) the dielectric scaffolding is manufactured using a low-cost FDM printer (model Anycubic Mega SE). The diameter of the nozzle is 200 μm and the adopted filament is polylactic acid (PLA, $\epsilon_r = 2.7$ and $\tan\delta = 0.008$). The conductive strips of the lines and the ground plane are painted using a colloidal silver paste that solidifies at room temperature (model PE16031 Colloidal Silver from Ted-Pella [45], $\sigma = 1 \times 10^6$ S/m). The linewidth was assessed using an optical microscope. The results are shown in Fig. 8. The extruded 3-D-printed patterns are composed of adjacent parallel lines so that the border is smooth. The major source of error is represented by the 3-D-printed scaffolding; an error in the linewidth comparable with the thickness of a single line (about 200 μm) has been observed. Nevertheless, for a given sample orientation and geometry, the error is systematic and can be partially pre-compensated in the model. In Fig. 7(b), the dielectric scaffolding is manufactured using stereolithography (SLA), while the metallization is manufactured with the colloidal silver paste. The adopted material is the Clear material from Formlabs [46]. The surface roughness of this sample is measured with an atomic force microscope, as shown in Fig. 9. An average surface roughness Sa of 180 nm is obtained, which is similar to the surface roughness of the 3-D-printed dielectric [41]. The root-mean-square roughness Sq is 250 nm. The thickness of the metal traces on both samples was measured with a caliper, and in both cases, an average value of 80 μm was obtained.

The main advantages of this technique are that it can be used to metallize both flat and curved surfaces, even with high surface roughness, without any epoxy-based primer

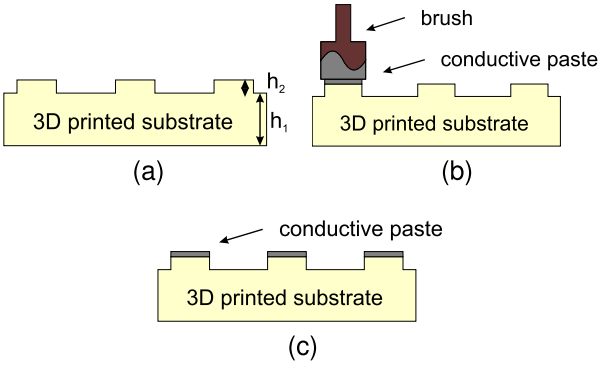

Fig. 6. *3-D printing-based embossed-surface patterning technique. (a) 3-D-printed embossed surface. (b) Conductive paste application. (c) Complete prototype with selective metallization.*

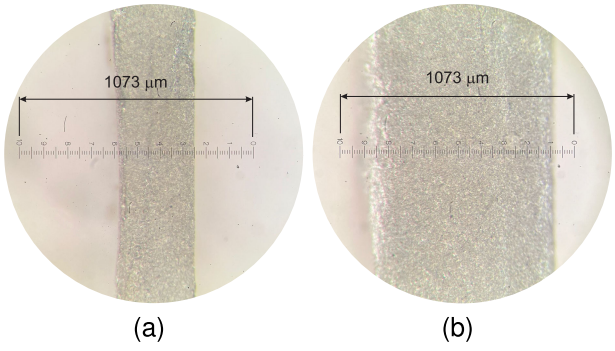

Fig. 8. *Optical microscope image of microstrip lines manufactured with the 3-D printing-based embossed-surface patterning (substrate: PLA). (a) Nominal linewidth: 0.5 mm (measured linewidth: 343.2 μm). (b) Nominal linewidth: 1 mm (measured linewidth: 836 μm). In both cases, the ruler each scale division is 10.725 μm.*

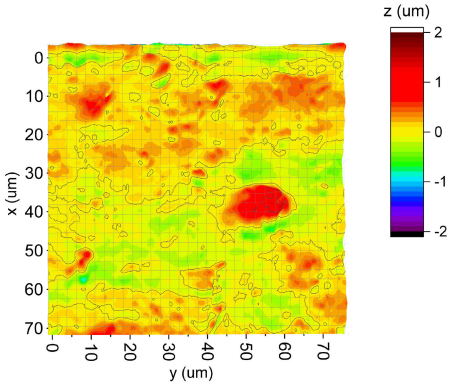

Fig. 9. *Atomic force microscope image of the microstrip line manufactured with the embossed-surface process on the Clear substrate (SLA). Sa = 180 nm and Sq = 250 nm.*

layers; no masks nor stencils are required for the metal deposition, and more generally, the pattern resolution is solely dependent on the 3-D printing process, while no other high precision tools are needed. The disadvantages, however, are that surface-mounted components cannot be soldered on the metal traces (epoxy resins are needed) and that based on the present technological advances, only manual deposition processes are envisioned, meaning that only limited control of the trace thickness is possible. However, as long as the metal thickness is larger than the skin depth, the impact of thickness variations on the signal propagation is limited.

Fig. 10 shows the photograph of the proof-of-concept prototype of an ultrawideband microstrip crossover developed with the afore-described technique. The crossover consists of an overpass and an underpass in microstrip technology obtained by cutting and bending the substrate, first presented in [41]. The dielectric scaffolding is PLA (manufactured using FDM), and the metallization is manufactured using silver colloidal paste. From a visual inspection, it is clear that the surface roughness is not uniform, and it increases significantly in the presence of suspended and curved parts.

The measured S-parameters are shown in Fig. 10. The crossover features an excellent performance of up to about 8 GHz. The input reflection coefficient of all ports is below -13 dB, while the coupling coefficient is below -35 dB. The transmission coefficient increases with frequency, and it is equal to -2.3 dB at 6 GHz (line length: 5 cm). The performance deterioration at higher frequencies is mostly due to the high surface roughness of the dielectric.

In the reported examples, the colloidal silver paste is applied to 3-D-printed scaffoldings with a large Young's modulus (the PLA filament has an elastic modulus of about 3000 MPa [47], while the Clear resin has an elastic modulus of 2750 MPa and an elongation break of 8% [46]). When subjected to limited bending (i.e., a fraction of millimeters), no resistivity increase was observed over tens of cycles. However, this paste is not indicated for flexible electronics since it is subject to the occurrence of cracks.

C. Electroplating and Electroless Plating

Popular techniques used to metallize 3-D-printed components are electroplating and electroless plating [48]. In both cases, first, the component is 3-D-printed using dielectric materials with techniques such as SLA or FDM. Then, a conductive layer is deposited on the dielectric surface. In electroplating, the metal layer is deposited by electrolysis. The surface to be coated is made conductive (either applying a conductive paint or by physical sputtering); then, it is immersed in an acid solution of copper sulfide. The copper is deposited by connecting a copper rod to the positive side of a battery, connecting the negative pole to the surface to be covered, and applying an electrical current. This technique leads to a good adhesion of the metallization and good conductivity (about 1×10^6 S/m), although it leads to a moderate surface roughness [49].

In electroless plating, no current is applied, and metal ions are deposited on a catalytic surface thanks to a reducing agent [50], [51]. The characteristics of the deposited Cu film are similar for the two techniques, although some differences exist; for instance, electroplating is characterized by a higher yield, while electroless plating can be applied also to nonconductive surfaces.

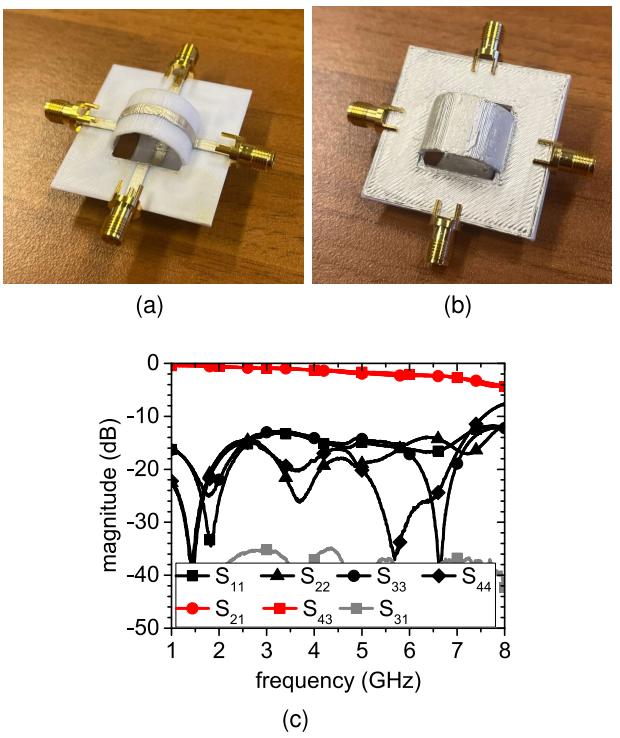

Fig. 10. *3-D microstrip crossover. (a) Top view. (b) Bottom view. (c) Measured S-parameters. Main circuit parameters: $h_1 = 0.8$ mm, $h_2 = 0.3$ mm, and $w_{line} = 3$ mm.*

It is worth mentioning that conductive material used as a seed for copper plating can have reduced conductivity. In such cases, this technique can be used for guiding structures in which the electromagnetic signals propagate above the copper layer and not below, to avoid high conduction loss.

Although these techniques are mostly used for waveguides and other all-metal RF components, attempts to achieve selective metallization have been made. For instance, in [53], two metal patterning processes are proposed: one based on a damascene-like approach and the other based on a 3-D-printed bilayer liftoff. In the first approach, trenches are 3-D-printed in the areas to be metallized. A thin layer of titanium (60 nm) is sputtered to make the surface conductive. Then, a layer of copper (0.5 μm) is deposited, and the metal layer is mechanically removed from the protruding areas of the surface. According to the second process, a spacer layer (uncured) is sandwiched between the proper 3-D-printed substrate and a sacrificial 3-D-printed area. All surface is metallized, and finally, the sacrificial 3-D-printed area above the spacer layer is removed. In [52], the thickness of the metal is increased to 5–6 μm using copper electroplating and the selective metallization is achieved with the damascene-like process.

This technique was used to manufacture microstrip components with an air substrate. The main process steps are shown in Fig. 11. In particular, the two metal layers of the microstrip line (i.e., the strip and the ground plane) are manufactured on two separate 3-D-printed layers with the damascene-like process. One of the layers is equipped with holes and the others are equipped with pillars, and the two layers are snapped together with the copper-coated sides facing each other, so as to implement an air substrate-based microstrip component. In Fig. 12(a), a 50-Ω microstrip line manufactured with the damascene-line fabrication process for air substrate-based microstrip components is shown. The 3-D-printed dielectric material is VeroWhitePlus, and the thickness of the substrate is 2 mm. The air gap between the two metal layers is 2 mm. The S-parameters of the microstrip line are shown in Fig. 12(b). The line shows an input reflection coefficient below -10 dB up to 5 GHz and a transmission loss of 0.17 dB/cm at 4 GHz.

Alternatively, a dual-extruder FDM printer has been used, where nonconductive and conductive films are deposited on the same component. Both electroplating [54] and electroless plating [51] have been used to metallize the areas corresponding to the conductive filament. In [55], a cold spray gun mounted on a programmable multiaxis robot arm was used instead of the conductive filament to deposit the conductive pattern for subsequent plating. Nevertheless, the components manufactured with these techniques (mostly lines and inductors) have been tested only in dc or up to 100 MHz.

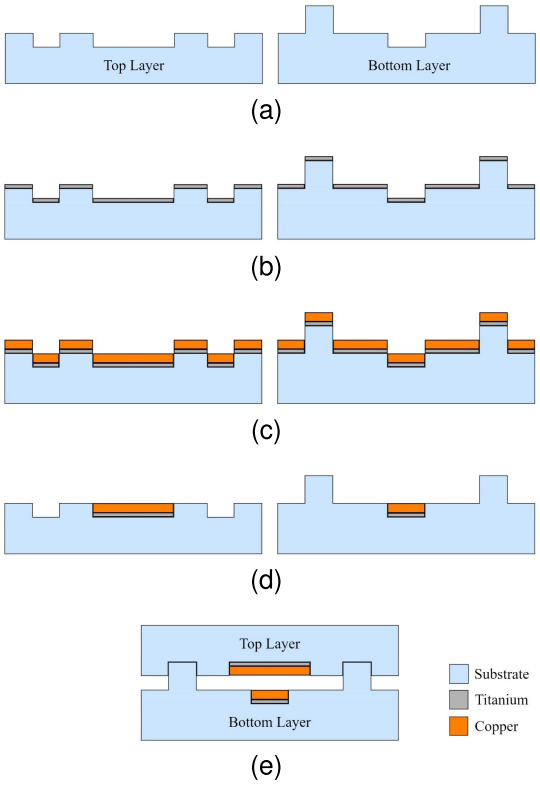

Fig. 11. *Process steps to manufacture air substrate-based microstrip components with electroplating. (a) Dielectric scaffolding of the two layers is 3-D-printed (tranches are manufactured in correspondence with the desired metal patterns). (b) Thin layer of titanium is sputtered on the whole surface to improve the copper adhesion. (c) Copper is first sputtered and then grown with copper electroplating. (d) Metal outside the tranches is mechanically removed. (e) Two layers are snapped together. After [52].*

D. Liquid Metal

The liquid metal technique leverages the capability of 3-D printing techniques, such as FDM and SLA, to manufacture embedded conductive structures. A dielectric scaffolding with small void channels (diameter below 1 mm) can be manufactured with 3-D printing so that the channels can be filled with liquid materials. This approach has been used to manufacture microfluidic channels for lab on chips and similar sensing solutions [56]. By filling the channels with conductive liquids, this technique can be used in RF applications to manufacture reconfigurable antennas [57], resonant structures [58], switchable metasurfaces [59], and coaxial transmission lines [60], [61], among others.

In [58], the dielectric mold is manufactured using multijet printing (printer model ProJet HD3000). To accurately control the diameter of the channels, a sacrificial material is first printed in the void areas, and then, it is removed with a mineral oil bath. The liquid metal paste injected in the channels is a silver suspension that solidifies at room temperature (Pelco 16040-30). However, the quality and

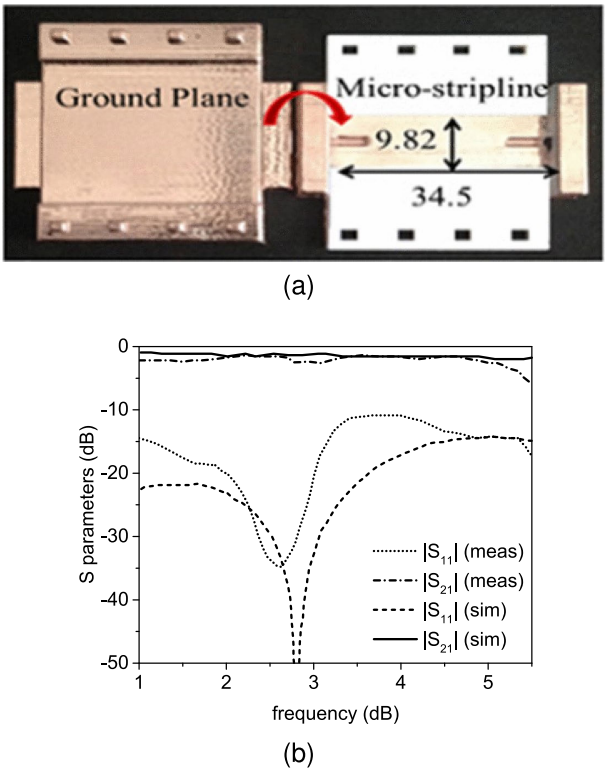

Fig. 12. *Air substrate-based microstrip line manufactured with the damascene-like process. (a) Photograph of the prototype and (b) S-parameters [52].*

thickness control of the metal structure has some limits; as the silver suspension shrinks after solidification, paste injection must be repeated, and in any case, channels are not fully filled (a volume-filling ration of 68.7% was observed after five filling steps). In addition, channel diameters below 600 μm could not be filled.

Eutectic gallium indium (EGaIn) is a metal alloy, which is liquid at room temperature [62]. Due to its low toxicity, high conductivity ($\sigma = 3.4 \times 10^6$ S/m), and flowability (it has been used to fill channels greater than 100 μm [63]), it can be conveniently pumped into microchannels and can be used as inner conductor for RF components in coaxial technology. Due to its stretchability, it has also been used to manufacture stretchable electronics in wearable applications [64].

By varying the diameter of the inner channel of the 3-D-printed dielectric scaffolding, this approach can be used to manufacture RF circuit components in coaxial technology with variable line impedance. The main process steps are shown in Fig. 13(a)–(c). First, the dielectric scaffolding of a coaxial line is 3-D-printed. In the reported example, SLA is used. In SLA, liquid photoreactive resins are laser-cured layer by layer, to yield solid objects with arbitrary shapes. Then, the channel is filled with EGaIn and two subminiature version A (SMA) connectors are attached to the extremes of the line. Channel filling can be performed using peristaltic pumps (see, for instance, [60]). Finally, the exterior of the dielectric scaffolding is coated with a colloidal silver paste, which solidifies at room temperature ($\sigma = 1 \times 10^6$ S/m). This way, the process does not involve any curing steps. In [60], the external metallization is manufactured using electroless silver plating.

The characteristic impedance Z_c of a coaxial line depends on the ratio of the radius of the inner conductor r_1 to the radius of the outer conductor r_2 (corresponding to the inner and outer radii of the dielectric scaffolding) as follows:

$$Z_c = \frac{\eta}{2\pi} \ln\left(\frac{r_2}{r_1}\right) \tag{2}$$

where $\eta = (\mu/\epsilon)^{1/2}$ is the intrinsic impedance of the dielectric medium and μ and ϵ are its complex permeability and permittivity, respectively. Therefore, once the other diameter of the cylinder is fixed, the line impedance can be controlled by changing r_1, which makes it possible to manufacture even complex RF components with a few steps [61]. Fig. 14 shows two channels with different diameters manufactured with SLA 3-D printing.

Fig. 13(d) shows the S-parameters in the frequency range of 1–20 GHz of one piece of coaxial transmission line manufactured with the afore-described technique. The adopted resin is the Clear material V4 [46], which has a permittivity of 2.7 and a loss tangent of 0.03 at 12 GHz [65]. The metal used for the inner conductor is an EGaIn alloy from Sigma Aldrich [66], while the outer conductor is manufactured with colloidal silver (model Pelco 16031 from TedPella [45]). The insertion loss of a 2-cm line is about 2.4 dB at 20 GHz, while the return

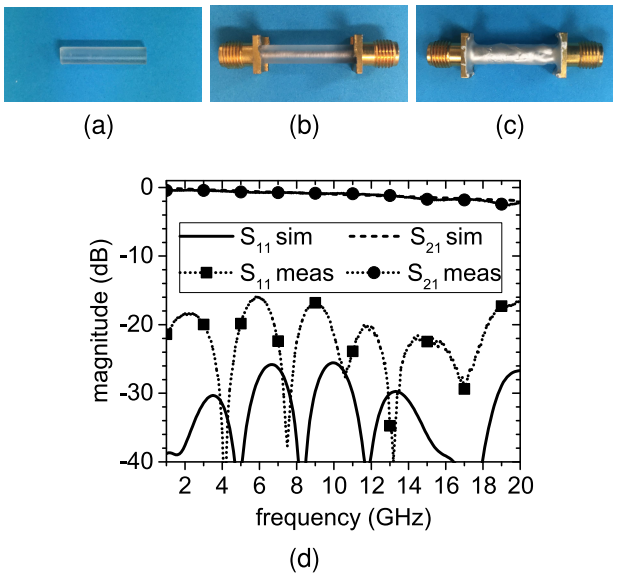

Fig. 13. *Additively manufactured coaxial line [61]. (a) 3-D-printed dielectric. (b) Prototype before colloidal silver deposition. (c) Complete prototype. (d) S-parameters.*

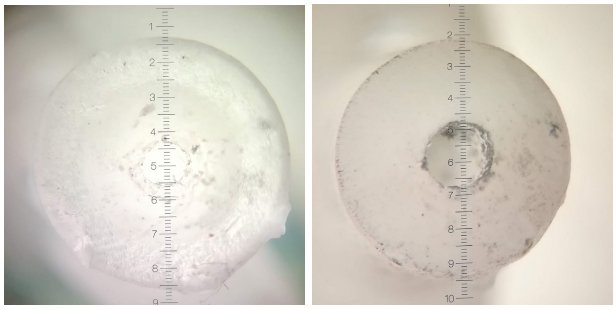

Fig. 14. *Photographs at microscope of 3-D-printed channels. (a) Measured diameter of the channel is 0.656 mm. (b) Diameter of the channel is 1.029 mm. Each scale division corresponds to 57.2 μm [65].*

loss is higher than 16 dB in all bands, thereby proving the capability of such technique to the manufactured RF components up to 20 GHz [65]. In comparison, in [60], an insertion loss of 0.03 dB/cm is reported at 10 GHz for a standard RG-142 coaxial cable.

III. EXAMPLES OF SELECTIVELY METALLIZED ANTENNAS

Antennas are key components of IoT nodes and, more generally, any transponder. As they usually occupy a significant portion of the transponder, they have an impact on its overall conformability, weight, and cost. Being able to manufacture antennas with low-cost technologies applicable to unconventional materials, while optimizing their radiation properties, is of paramount importance to achieve a good integration of the transponder with the items to be monitored while establishing a reliable wireless link. A few examples of antennas and beamforming networks manufactured with the described techniques are illustrated in the following. All materials are first electromagnetically characterized, and the designs are based on full-wave simulations.

A. Bendable and Compressible Antenna Systems

Liquid metal in combination with 3-D printing was used to manufacture a variety of antenna types [57], [67], [68]. Due to its stretchability, EGaIn can be used to guarantee electrical continuity in bendable structures [69]. In addition, its good flowability can be used to dynamically fill and unfill channels [70], thereby leading to reconfigurable circuits.

In [57], a compressible antenna system is presented. The dielectric scaffolding, manufactured with SLA using a flexible material (flexible resin from Formlabs), includes a Voronoi structure and two microfluidic channels. By filling either of the two channels, a zigzag (linearly polarized) or a helix (circularly polarized) antenna is implemented, working at different frequencies (3 and 5 GHz, respectively). The proof-of-concept prototype is shown in Fig. 15(a). In addition, thanks to the 3-D-printed Voronoi structure that helps relief the stress, the antenna can be mechanically compressed, which is further leveraged to change its radiation pattern. As shown in Fig. 15(b) and (c) for the zigzag antenna, when the antenna is compressed, its radiation pattern is more omnidirectional, while the antenna features a higher directivity when it is uncompressed.

In [68], a miniaturized inverted-F antenna (IFA) operating at 885 MHz for wearable applications is presented. The scaffolding of the antenna is 3-D-printed using FDM (Ninjament filament is adopted), and the metal structure is injected in the channels encapsulated in the dielectric scaffolding using EGaIn. A photograph of the prototype is shown in Fig. 16(a). The antenna is measured using an SMA connector, where the internal conductor is connected to the radiating element and the outer conductor is connected to 50 $\times$ 50 cm flexible electrotextile sheet representing the ground plane of the antenna (a thickness of 0.08 mm and a sheet resistance of 0.05 Ω/sq), as shown in Fig. 16(b). A flexible foam is used to keep a constant distance between the radiating element and the ground plane. The antenna was tested under four different radii of curvature [see Fig. 16(c)]: $R1 = 18$ cm, $R2 = 14$ cm, $R3 = 8$ cm, and $R4 = 5$ cm. The input reflection coeffi-

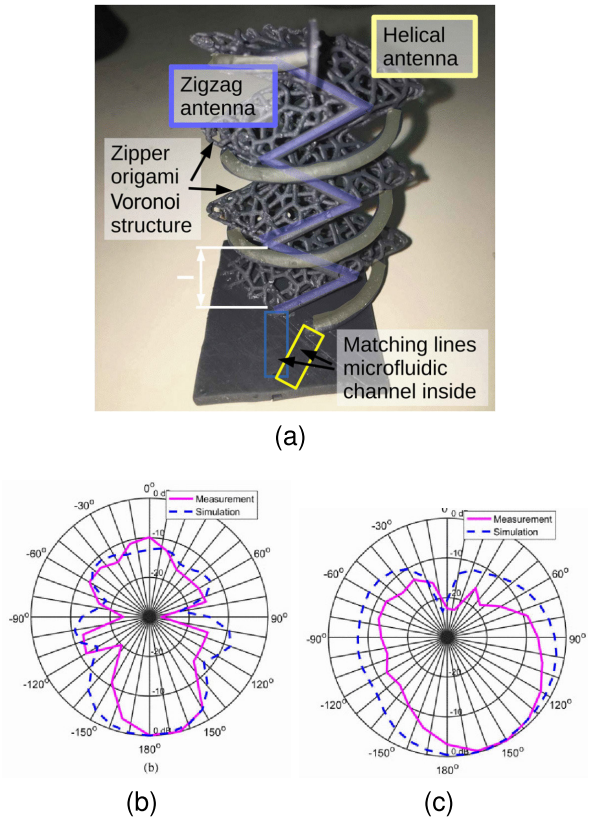

Fig. 15. *3-D-printed origami antenna. (a) Prototype. Normalized radiation pattern of (b) uncompressed and (c) compressed zigzag antenna [57].*

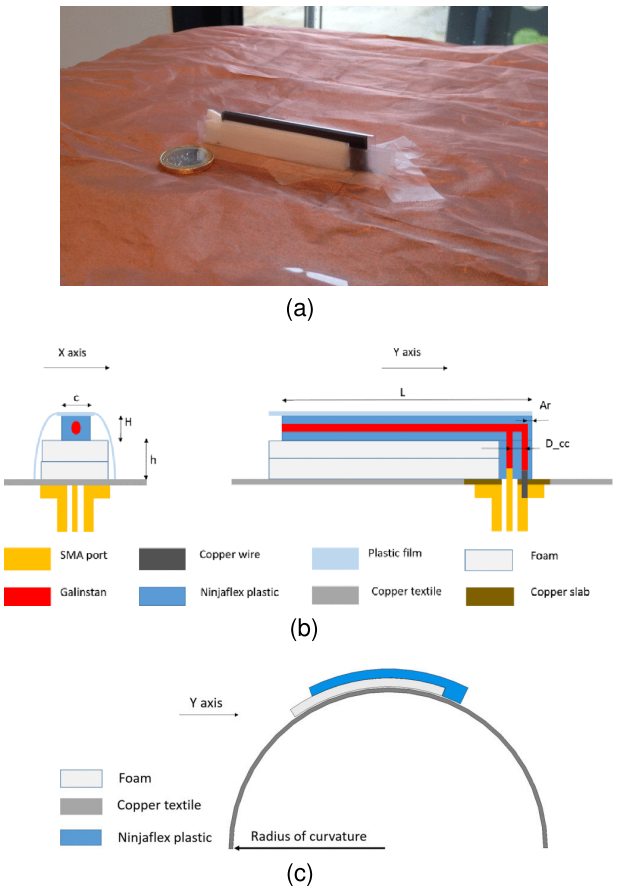

Fig. 16. *Bendable IFA antenna based on FDM and liquid metal [68]. (a) Photograph of the manufactured prototype. (b) Antenna structure. (c) Sketch of the antenna under bending. The main antenna parameters: $L = 66.5$ mm, $A_r = 1.3$ mm, $D_{cc} = 2.5$ mm, $c = 3$ mm, $H = 3$ mm, and $h = 11.5$ mm.*

cient of the antenna was demonstrated to be stable with frequency, while a maximum variation of the broadside gain of about 3.5 dBi is reported.

B. 3-D Butler Matrix

As anticipated in Section II-D, liquid metal can enable the manufacturing of RF components in coaxial technology. Indeed, the dielectric part of the coaxial cable can be 3-D-printed, while liquid metal can be used to fill the channels, thereby implementing the inner conductor. As an example, in [61], a 4 × 4 Butler matrix is manufactured. Fig. 17 shows the layout of the circuit. The matrix consists of four circular branch-line couplers and 50-Ω transmission lines, and it is designed to operate at 12 GHz. The input and output ports are equally spaced and placed in a row. The four 90° hybrids, labeled as B1–B4 in Fig. 17, are arranged to minimize the line length and area occupation: B1 and B2 are placed on the same plane, while B3 and B4 are placed one on a parallel plane above and the other on a parallel plane below the plane of the ports, respectively. The angles α and γ in Fig. 17 are designed so that the

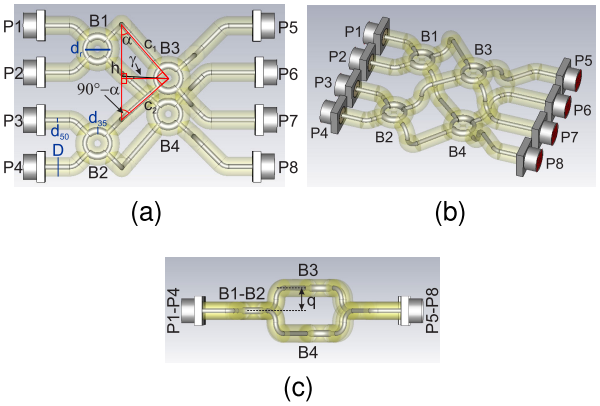

Fig. 17. *Layout of the 4 × 4 3-D-printed Butler matrix in coaxial technology. (a) Top view. (b) Perspective. (c) Side view. The main circuit parameters: $D = 4$ mm, $d_{50} = 1$ mm, $d_{35} = 1.55$ mm, $d_r = 5.3$ mm, $h = 19.6$ mm, $c_1 = 14.77$ mm, $c_2 = 12.88$ mm, $q = 5$ mm, $\alpha = 42.85°$, and $\gamma = 2.15°$. After [61].*

electrical length of the lines connecting B1 to B3 and B2 to B4 is 45° longer than those connecting B1 to B4 and B2 to B3 at the operating frequency, as requested by the Butler matrix circuit. The 35- and 50-Ω lines of the branch-line couplers are manufactured by varying the diameter of the inner channel representing the internal conductor of the coaxial line.

Fig. 18(a) and (b) shows the photographs of the proof-of-concept prototype at different manufacturing stages, while the magnitude and phase of the transmission coefficients related to port 1 are illustrated in Fig. 18(c) and (d) by way of example, while the complete S-parameters are

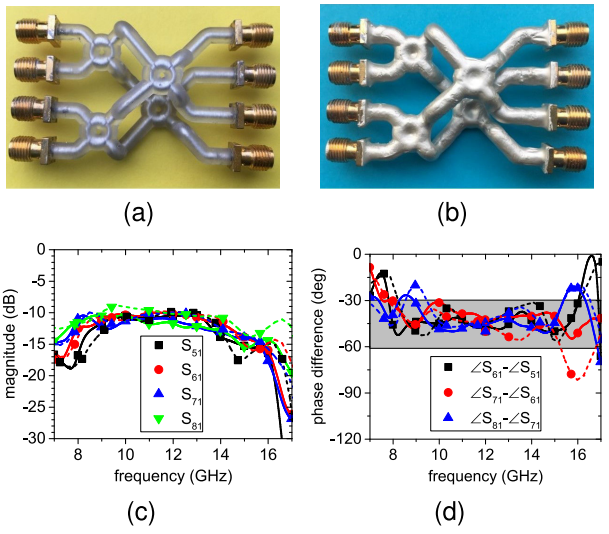

Fig. 18. *Fabricated Butler matrix prototype. (a) Before colloidal silver deposition, (b) complete prototype, (c) magnitude, and (d) phase difference of the transmission coefficients related to input port 1. Simulations are dashed lines and measurements are solid lines. After [61].*

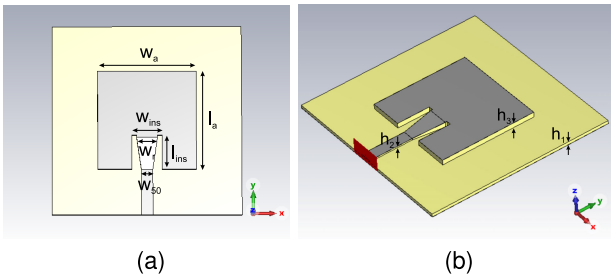

Fig. 19. *3-D-printed embossed-surface patch antenna layout. (a) Top view. (b) Side view. The main parameters are: $w_a = 26$ mm, $l_a = 26$ mm, $w_{ins} = 8$ mm, $l_{ins} = 8.7$ mm, $w_{50} = 3.1$ mm, $w_r = 5.6$ mm, $h_1 = 0.85$ mm, $h_2 = 0.4$ mm, and $h_3 = 1.35$ mm.*

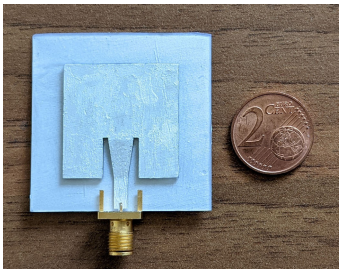

Fig. 20. *Photograph of the complete 3-D-printed embossed-surface patch antenna prototype. Area, including the ground plane: 40 × 40 mm.*

reported in [61]. An operating band between 11 and 13.6 GHz was observed, in which the transmission coefficients are characterized by a magnitude and phase error of 2 dB and 15°, respectively, and the isolation between each couple of output ports is higher than 16 dB. Comparing the proposed solution with other state-of-the-art 3-D-printed and single-layer versions of the Butler matrix (i.e., based on low-cost technologies), we observed that it features a larger bandwidth while achieving a smaller footprint, as shown in Table 2.

C. 3-D-Printed Microstrip Antennas

When designing planar circuits, thin substrates are generally preferred for RF transmission lines to reduce radiation loss, while thicker substrates are generally preferred for microstrip antennas, as they lead to higher radiation efficiency and broader bandwidth.

Leveraging the flexibility provided by 3-D printing and relying on the embossed-surface patterning technique, a thick substrate for the antenna can be designed just increasing the thickness of the extruded pattern in correspondence with the antenna area. This way, thin microstrip lines, with low radiation loss, and thick microstrip antennas, with improved bandwidth and gain, can coexist on the same substrate. As an example, a microstrip square patch antenna is shown in Fig. 19. A ramp is used to connect the feedline to the patch while keeping the impedance matching. The thickness of the microstrip line increases linearly along the ramp, and the width of the line increases as well to keep the characteristic impedance of the line equal to 50 Ω.

The photograph of the manufactured antenna is shown in Fig. 20. The results of the full-wave simulations and the obtained experimental results are shown in Fig. 21. In Fig. 21(a), we compare the simulated input reflection coefficient of the proposed antenna with the reflection coefficient of a patch with the same thickness as the microstrip feedline ($h_1 + h_2 = 1.25$ mm) without the ramp [the "flat" antenna, as defined in the legend of Fig. 21(a)], with the same minimum $|S_{11}|$. The simulated −10-dB fractional bandwidth of the proposed antenna is 4.7%, while the one of the "flat" antenna is 3%. The manufactured antenna has a measured input reflection coefficient of −18 dB at 3.5 GHz, as shown in Fig. 21(a), and a −10-dB fractional bandwidth of 4.3% (the slight bandwidth reduction with respect to the simulated value is due to the worsening of the impedance matching). A downshift of the minimum reflection coefficient of about 30 MHz is observed as well, which can be attributed to small manufacturing inaccuracies and small variations in the permittivity of the 3-D-printed dielectric material.

The antenna is linearly polarized, as shown in Fig. 21(c). The cross-polar component is 20 dB below the co-polar component at the antenna broadside direction. The half-power beamwidth of the antenna on the H-plane

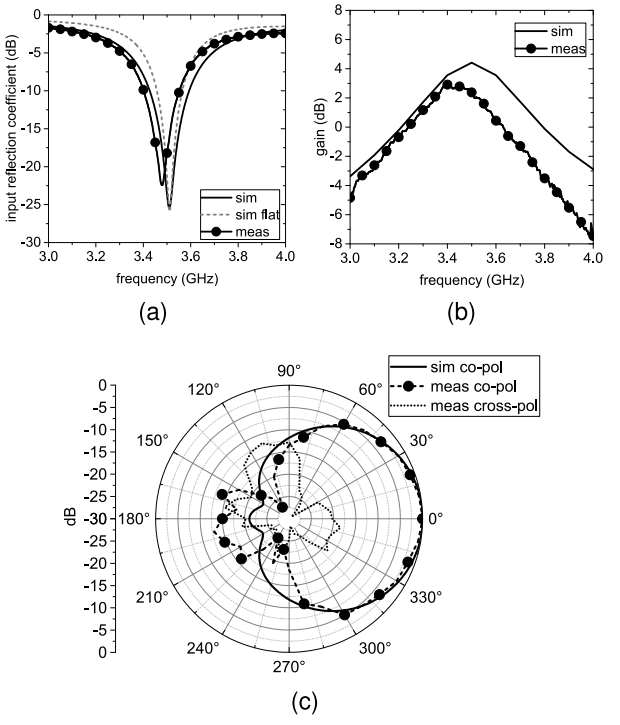

Fig. 21. *3-D-printed embossed-surface patch antenna performance. (a) Input reflection coefficient. (b) Broadside gain. (c) H-plane radiation patterns.*

Table 1 Room-Temperature Selective-Metallization Technologies: State of the Art

Technology	Conductor	Conductivity (S/m)	Metal thickness (μm)	Skin Depth @ 1 GHz (μm)	Dielectric	RMS rough. (nm)	Min. line width (μm)
Metal Foil	Copper Foil	5.8×10^7	35	2.06	PHBV[1] Cardboard Paper	263	200
Embossed Surface	Colloidal Silver	1×10^6	80	15.9	PLA[2](FDM[3]) Clear (SLA[4])	250	343
Liquid Metal	Gallium Indium	3.4×10^6	> 100	8.6	Clear (SLA[4]) VisiJet Crystal M3 Cyanate Ester	/	100
Sputtering + Electroplating	Titanium and Copper	/	5-6	/	VeroWhitePlus	/	/

[1] Poly(3-hydroxybutyrate-co-3-hydroxyvalerate)
[2] Polylactic acid
[3] Fused deposition modeling
[4] Stereolithography

is 81°. At resonance, the proposed antenna has a total radiation efficiency of 52%, which is significantly higher than the 37% efficiency of the reference "flat" antenna. In addition, despite the limited extension of its ground plane, the antenna radiates with a front-to-back ratio of 15 dB.

Finally, the broadside gain versus frequency is shown in Fig. 21(b). The antenna features a gain of 2.4 dBi at 3.5 GHz and a maximum gain of 3.4 dB at 2.92 GHz. Discrepancies between simulations and measurements are attributed to manufacturing tolerances and nonidealities of the measurement setup (such as the presence of cables and connectors).

In [52], an air substrate-based microstrip patch antenna and other antennas and resonators were manufactured with the damascene-like process described in Section II-C. Photographs of the antenna prototype are shown in Fig. 22. The thickness of the air gap is 2 mm, and the antenna is connected to an SMA connector. The antenna, operating at 5 GHz, has a −10-dB fractional bandwidth of 2.45% and a peak gain of approximately 6 dBi. In [52], other antennas and resonators have been presented as well, demonstrating the suitability of this fabrication process to manufacture passive RF components up to 6 GHz.

D. Dual-Layer and Multilayer Antennas

The metal foil tape technology can be used, among other things, to manufacture high-resolution flexible antennas.

Table 2 Comparison With the State of the Art [61]

ref.	tech.	freq. (GHz)	ϵ_r	volume (λ_0^3)	mag. err. (dB)	phase err. (deg.)
this work	3D prin.	$11 - 13.6$	2.7	$1.7 \times 1.3 \times 0.56$	2	15
[65]	3D prin.	12	2.7	$1.8 \times 2.1 \times 0.65$	$2^\dagger$	$5^\dagger$
[71]	s. layer	6	2.2	$3.7 \times 1.5 \times 0.02$	0.8	6
[72]	s. layer	28	6.2	$1.7 \times 1.8 \times 0.02$	4.7*	16*
[73]	s. layer	27.5−28.3	2.2	$2.8 \times 3 \times 0.02$	/	14.5*

∗ Value from simulation results. † Value from partial results.

In [74], a dual-layer antenna system consisting of two nested tapered annular slots working at harmonic frequencies (i.e., at $f_0 = 1.2$ GHz and $2f_0 = 2.4$ GHz) is demonstrated. The photograph of the antenna prototype is shown in Fig. 23(a) and (b). The antenna system is manufactured on photographic paper (a thickness of 370 μm, a permittivity of 2.55, and a loss tangent of 0.05) using copper foil tape. The slots are the result of the intersection of an ellipse and a concentric circle and are nested one inside the other to reduce their area occupation. The proximity-coupled microstrip feedlines are placed on the other side of the substrate in such a way that they utilize the metal surface between the two slots as a common ground plane. The feedline of each antenna terminates on a circular disk stub with a radius tuned to match the antenna to a 50-Ω impedance. The slot length is approximately equal to a guided wavelength at the operating frequency (resonant slot). The two slots are linearly polarized and radiate with orthogonal polarization. They feature a −10-dB fractional bandwidth of 22% and 12%, as shown in Fig. 23(c). In the E-plane, the half-power beamwidth is 81° for the f_0 slot and 73° for the $2f_0$ slot, and their respective broadside gain at center frequency is

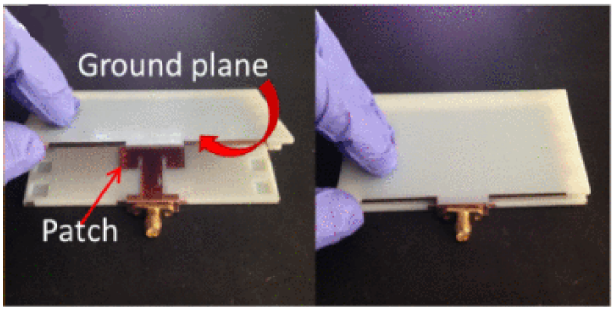

Fig. 22. *Photograph of an air substrate-based microstrip patch antenna based on the damascene-like fabrication process. Area of the prototype, including the ground plane: 124 × 54 mm. After [52].*

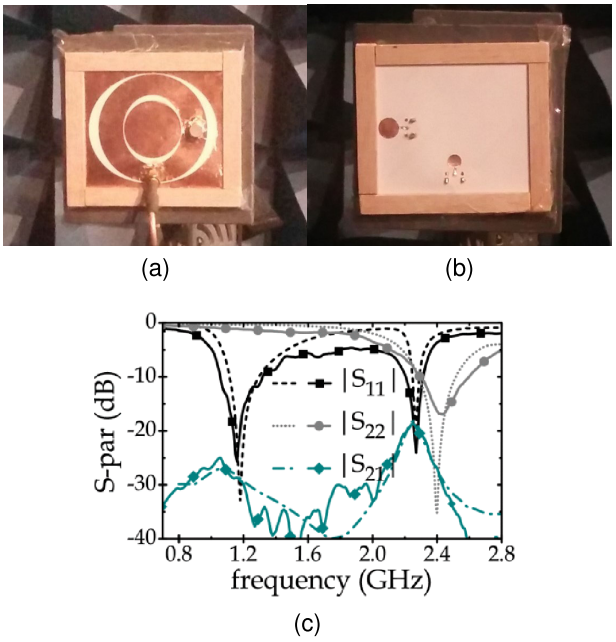

Fig. 23. *Dual-layer nested annular slot antennas. (a) Top layer, (b) bottom layer, and (c) S-parameters [74].*

3.3 and 3 dBi. The eccentricity of the ellipse can be used to tune the fractional bandwidth of the antenna (a similar approach was used in a multiband rectenna in [36]).

Besides enabling double-layer circuits, the metal foil tape technology described in Section II-A can be used to manufacture multilayer circuits. As for single- or dual-layer circuits, each metal layer is manufactured separately; then, the layers are attached to the respective substrates, which are finally stuck together. This way, we can easily assemble flexible multilayer circuits, even based on heterogeneous substrates.

In [75], this technique was adopted to manufacture the front end of a Doppler radar working at 24 GHz [75]. The stack up of the circuit is shown in Fig. 24(a). Overall, the circuit consists of three metal layers and two layers of photographic paper: one metal layer (antenna side) is used for the antenna, one (active side) is used for the mixer and branch-line coupler, and one is used for the common ground plane. A photograph of the antenna prototype is shown in Fig. 24(b). The antenna consists of an array of 2×2 microstrip patch antennas. The feed network consists of three T junctions and two quarter-wave impedance transformers. The array is connected to the rest of the front end with a via-through manufactured by soldering a 0.2-mm copper wire to both the top and the bottom layer. The antenna has a gain of 7.4 dBi, has an impedance bandwidth of 540 MHz and a radiation efficiency of 35%, and features a half-power beamwidth of 48°, as shown in Fig. 24(c).

In [77], a multilayer dual-port dual-frequency patch antenna for harmonic transponders is presented. In this case, the substrate used for the antenna is cardboard (a thickness of 2.5 mm, ϵ_r of 1.35, and a loss tangent of 0.02), while the substrate used for the circuitry is a film of PLA, a bioplastic derived from corn starch that is used also as thermoplastic filament in FDM (a thickness of 0.3 mm, ϵ_r of 2.8, and a loss tangent of 0.008). A rectangular patch is placed on the cardboard. The antenna is designed so that its long side resonates at the fundamental frequency $f_0 = 2.4$ GHz, while the short side resonates at the second harmonic $2f_0 = 4.8$ GHz. The patch is electromagnetically coupled to the two microstrip feedlines manufactured on the PLA film through two H-slot apertures on the ground plane placed between the cardboard and the PLA substrates. This way, there are no vias between the heterogeneous materials, which facilitates the antenna integration. Fig. 25(a) shows the stackup, while Fig. 25(b) and (c) shows the top and bottom layers of the manufactured prototype, respectively. The maximum gain of the antenna at f_0 is 3 dBi, while its gain at $2f_0$ is 8.2 dBi. This demonstrates the capability of the copper foil tape technology to manufacture multilayer RF components up to the K band on a variety of materials.

IV. WIRELESS SENSING

By leveraging both the mechanical and electromagnetic properties of unconventional materials, the described manufacturing processes, and antenna solutions, complete wireless transponders for sensing have been presented. The aim of this research line is to develop wireless sensing systems, where the transponders can be easily integrated

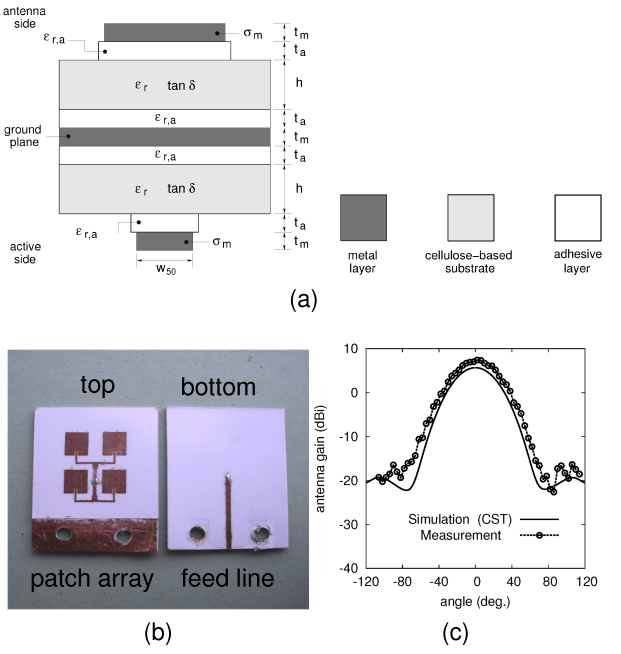

Fig. 24. *Multilayer 24-GHz antenna array on photographic paper. (a) Circuit stack up, (b) photograph of the prototype, and (c) H-plane radiation pattern at 24.15 GHz. The circuit area is 35 × 28 mm. After [76] and [75].*

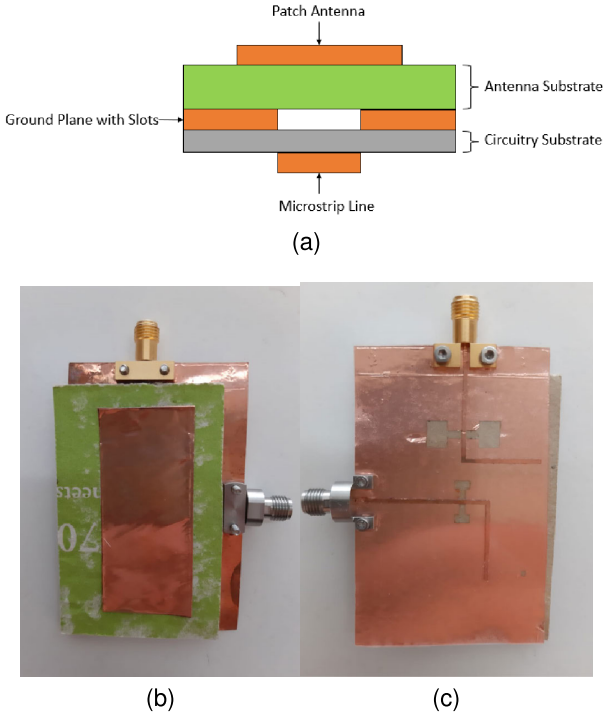

Fig. 25. *Multilayer dual-band dual frequency antenna. (a) Circuit stack up, (b) top layer, and (c) bottom layer [77].*

with common objects and are able to operate in a variety of environments, as requested in many IoT applications. Here, some of the solutions in the state of the art are reported and discussed.

A. Harmonic Transponders

Harmonic transponders are a particular type of backscatter radios. As the latter ones, they backscatter the RF signal transmitted by a reader. However, while the backscattered signal of traditional backscatter radios lays in the same band as the interrogating signal (generally backscatter radios modulate the impinging signal in amplitude or phase), harmonic transponders backscatter the signal at higher harmonic frequencies (generally at the second harmonic). This way, the receiver is tuned to a different band with respect to the transmitted signal and does not suffer from self-jamming problems. These transponders are particularly interesting for IoT applications for their robustness to clutter, simplicity, and low cost.

In their simplest form, harmonic transponders include two antennas, working at f_0 and $2f_0$, or a dual-band antenna, and a nonlinear component [78]. Generally, surface-mounted components are used for the diode and eventual other passive components, although some attempts to make an all-organic harmonic transponder have been reported. In [79], in particular, a harmonic tag working in the near field at $f_0 = 7.5$ MHz is reported. Two nested resonant coils are manufactured with copper foil on paper, while the diode is manufactured by depositing a pentacene layer between the anode and cathode contacts on a polyethylene terephthalate (PET) substrate. However, the high conversion loss (higher than 52 dB) limits the read range of the transponder. Among other applications, harmonic transponders have been used for motion sensing [80], vital signs monitoring [81], victim rescue [82], and tracking [83], [84].

The second harmonic can be generated using passive frequency doublers. As shown in Fig. 26(a), the basic circuit includes a series-connected low-barrier Schottky diode, two quarter-wave harmonic stubs (one closed in short circuit and the other in open circuit), and input and output matching networks, to ensure proper impedance matching with the antennas and eventual other circuit components of the transponder. When the sinusoidal input signal is distorted by the nonlinear resistance of the diode,

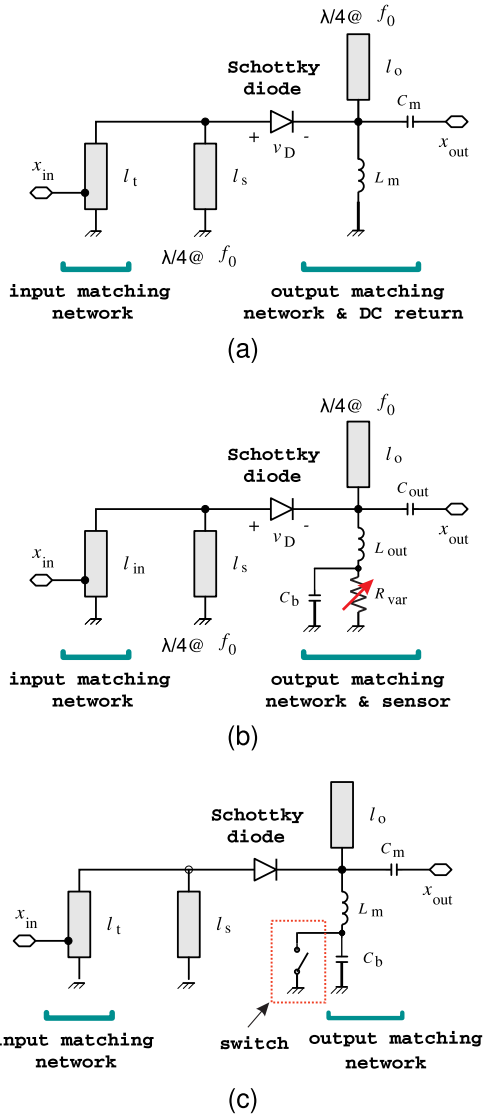

Fig. 26. *Schematic of passive frequency doublers for sensing. (a) Basic circuit. (b) Variable resistor. (c) Switch.*

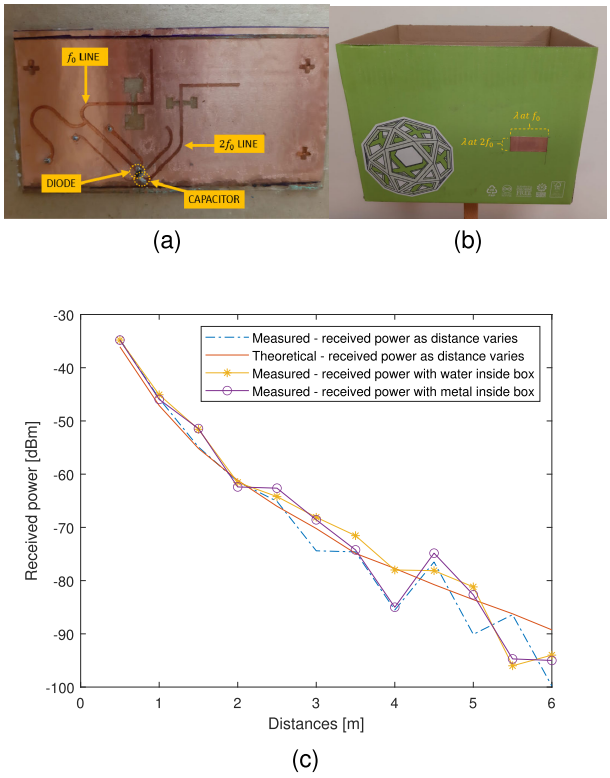

Fig. 27. ***Harmonic tag for parcel tracking. (a) Photograph of the PLA substrate, (b) photograph of the exterior of the box, and (c) backscattered second harmonic power versus distance [77].***

all harmonic components are generated, including the dc. To minimize the conversion loss of the doubler (defined as the ratio of power of the second harmonic delivered to the load to the available input power at the fundamental frequency), the diode is zero biased since the short-circuited quarter-wave stub connected at the diode anode and the inductor of the output matching network provide a dc return for the diode.

A variation of this circuit schematic has been studied, where a bypass capacitor is connected between the inductor and the ground, while a variable resistor (i.e., a transducer) is connected in parallel with the capacitor [see Fig. 26(b)]. This way, the inductor is virtually connected to the ground for the RF signal components, while the dc current flows through the resistor. It can be demonstrated that this makes the diode reverse biased, which in turn causes an increase in the conversion loss of the circuit [85]. In particular, the larger the resistor, the higher the conversion loss, which induces an amplitude modulation of the backscattered second harmonic signal. Alternatively, a switch can be connected between the inductor and ground, inducing a binary modulation of the backscattered signal [see Fig. 26(c)]. This mechanism has been used to measure temperature, pressure, rotational speed [85], and vibration [86], among others.

In [77], a harmonic tag for parcel tracking is presented. The tag is based on the multilayer antenna described in Section III-D, consisting of a dual-port dual-band aperture-coupled rectangular patch. The fundamental frequency is 2.4 GHz. The feedline associated with the f_0 port of the antenna is connected to the input port of the frequency doubler, while the feedline associated with the $2f_0$ port of the antenna is connected to the output port of the frequency doubler. This way, the microstrip feedlines and the frequency doubler are manufactured on the same metal layer. This layer and the ground plane with the slot apertures are attached to the two sides of the PLA film. The rectangular patch is attached to the cardboard on the exterior of the box and the circuit on the PLA is stuck on the interior of the box and it is aligned with the rectangular patch antenna, without any further manufacturing steps. Photographs of the transponder are shown in Fig. 27(a) and (b). Since the patch antenna has a ground plane, its radiation properties are minimally affected by what is placed inside the box. Fig. 27(c) shows the backscattered power received by the reader versus distance. We can see that the transponder can be read up to 6 m (transmitted power 25 dBm) regardless of the material of the objects placed in close proximity with the tag inside the box.

In [87], a 3-D-printed harmonic transponder for buried asset localization is presented. The transponder consists of a dual-band slot antenna and a diode and operates at the fundamental frequency of 2.55 GHz. The antenna is 3-D-printed with SLA using the Form 2 printer. The diode is inserted in a cavity during the printing process, with the pads exposed (no soldering is used to connect the diode to the antenna). Then, the complete 3-D-printed structure is metallized with titanium and copper (sputtering) and finally electroplated with copper. A photo of the manufactured prototype is shown in Fig. 28. The read range of the tag was up to 80 cm in air and up to 20 cm with the tag buried in the ground (a transmitted power of 13 dBm).

B. Paper and Cardboard-Based Disposable Harmonic Crack Sensor

Crack sensors are pivotal in a plethora of applications, ranging from structural health monitoring to anti-counterfeiting and industrial condition monitoring. Historically, crack detection is demanded to wired sensors or semiautomated systems that require periodic inspections from the operators [89]. However, the often significant extension of the structures and infrastructures to be monitored makes the installation and maintenance

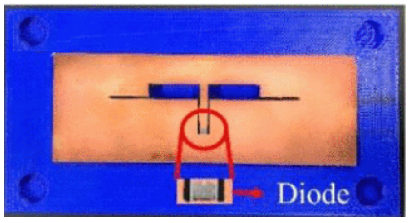

Fig. 28. ***Photograph of 3-D-printed harmonic tag. After [87].***

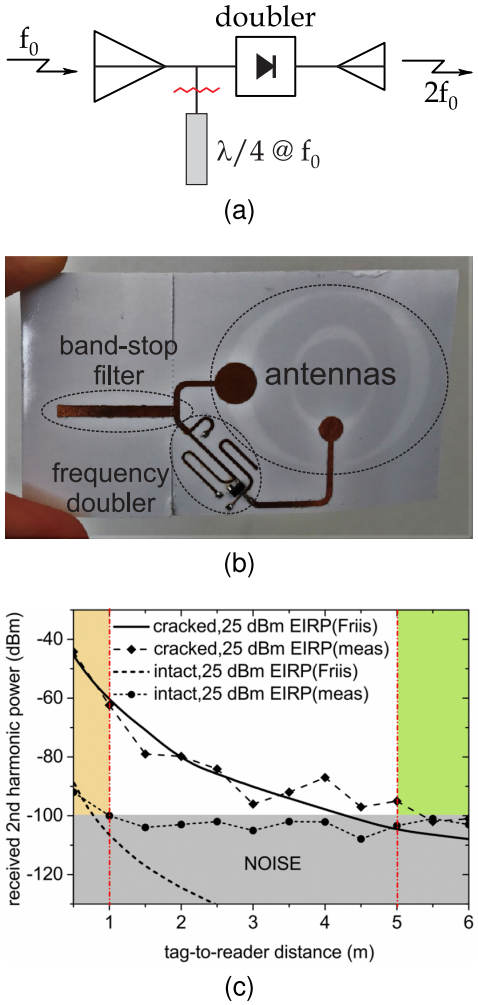

Fig. 29. ***Harmonic tag for crack sensing. (a) Schematic of the harmonic transponder, (b) photograph of the proof-of-concept prototype, and (c) measured received second harmonic versus tag-to-reader distance [88].***

of wired sensors impractical. For these reasons, several approaches have been studied to detect the occurrence of cracks using passive and wireless sensors [90], [91], [92], [93], [94], [95], [96].

In [88], a harmonic transponder for crack sensing is proposed. The schematic of the sensor is shown in Fig. 29(a). The sensor is equipped with an open-circuited quarter-wave stub at the input of the frequency doubler. As long as the transponder is intact, the stub short circuits the input signal gathered by the f_0 antenna. Therefore, ideally, no second harmonic is generated. On the other hand, if a crack occurs and the stub is torn off, the circuit operates like a basic harmonic transponder, and the received second harmonic signal acts as an alarm.

The crack sensor in [88] is manufactured on photographic paper. Cellulose-based materials are ideal substrates for this kind of sensor since they are prone to tear. A photograph of the proof-of-concept prototype is shown in Fig. 29(b). The tag, manufactured with the copper foil technology, is based on two nested annular slot antennas electromagnetically coupled to microstrip feedlines terminating with circular stubs, as described in Section III-D, and works at $f_0 = 2.45$ GHz. A read range up to 5 m with the tag in air was demonstrated with a transmitted power of 25-dBm effective isotropic radiated power (EIRP), as shown in Fig. 30(c).

A variation of the previous circuit is shown in Fig. 30. The schematic of the frequency doubler is modified to achieve a via-less circuit [see the circuit schematic in Fig. 30(a)]. Following the approach first presented in [97], a closed line path is used as the dc return to make the diode zero biased even in the absence of vias, while two quarter-wave open-circuited stubs are used to create the virtual ground for the fundamental and second harmonic components of the RF signal. Removing vias

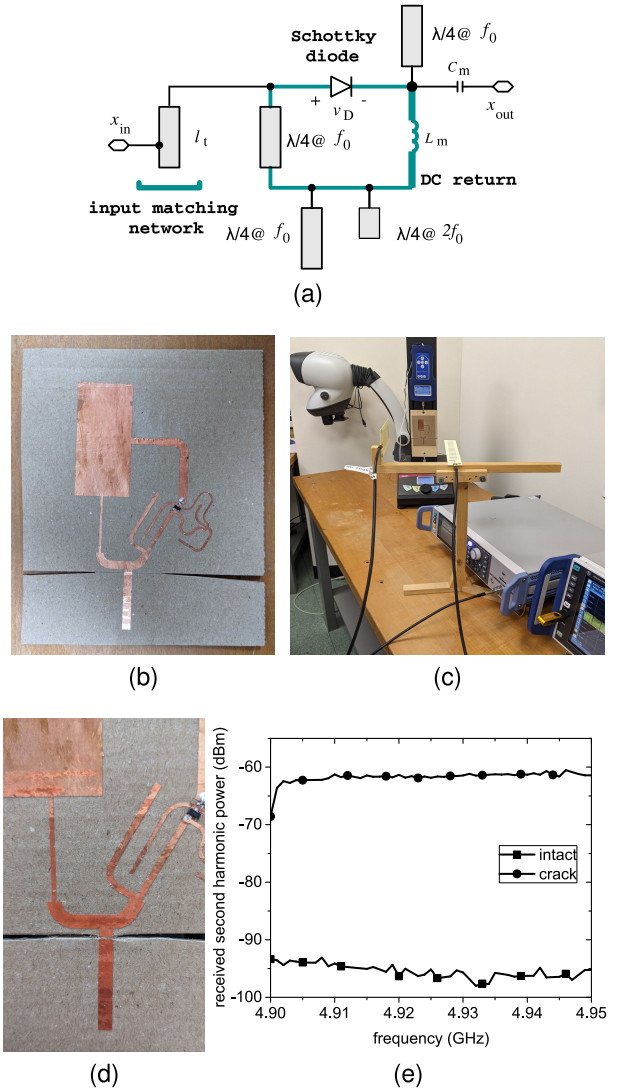

Fig. 30. ***Harmonic tag for crack sensing. (a) Schematic of the via-less frequency doubler. (b) Photograph of the proof-of-concept prototype on cardboard. (c) Photograph of the measurement setup. (d) Detail of the stub after break. (e) Received second harmonic power.***

Fig. 31. *Separated materials of the harmonic crack sensor for recycling: copper foil, cardboard, and surface-mounted components.*

reduces the manufacturing steps of the transponder and makes the metal traces easily separable from the substrate once the circuit must be disposed of, making it recyclable. The adopted substrate is cardboard (a thickness of 1.2 mm, a permittivity of 1.5, and a loss tangent of 0.02). The antenna system consists of a dual-port dual-band rectangular patch antenna.

The substrate is cut in proximity to the stub to ease the stub removal under strain. A photograph of the prototype is shown in Fig. 30(b). As proof of concept, a tensile force is applied to the transponder with a stator, as shown in Fig. 30(c). A dynamometer is used to measure the applied force. As expected, the sensor broke in correspondence with the stub [see Fig. 30(d)]. The received second harmonic, measured at a distance of 70 cm (transmitted power equal to 20-dBm EIRP, frequency of the transmitted signal swept between 2.45 and 2.475 GHz), is shown in Fig. 30(d). When the stub breaks, the backscattered signal increases by more than 35 dB at $2f_0 = 4.93$ GHz.

After the stub is torn off, the transponder cannot be used anymore as a crack sensor and must be disposed of. To recycle its components, we must first separate the metal from the cardboard. This can be done using acetone to remove the glue, which keeps the metal trace attached to the cardboard. Alternatively, the metal traces can also be mechanically peeled off. The surface mount device (SMD) components can be separated from the copper traces by applying hot air. The separated components of the crack sensor are shown in Fig. 31. It is worth mentioning that this process does not damage the SMD components that can be reused in other circuits.

C. Bimorph Paper-Al Cantilever

In [25], a bimorph paper-Al cantilever structure has been proposed as a humidity-sensitive microelectromechanical system (MEMS) capacitor. The cantilever is formed by an aluminum (Al) foil glued on top of a paper layer. In the presence of humidity, the paper relaxes its fibers. This means that the length of the paper layer increases (with respect to that of the Al layer) when humidity is absorbed, thus determining the cantilever deflection. Such a mechanism is used to control a capacitor formed by the cantilever itself (Al layer) and by a metal plate printed on a PCB. A microstrip notch filter is tuned by such a capacitance and used to detect the humidity variations.

The frequency response of the filter is measured with a vector network analyzer (VNA) and a series of macro photographs are captured in order to relate the MEMS capacitor movement to the filter frequency response, as reported in Fig. 32. The environment relative humidity (RH) is measured with a laboratory hygrometer and, at the beginning of the experiment, it was close to 40% (left panels). In these conditions, the bimorph cantilever is quite flat and the notch frequency is about 2.19 GHz. Then, a cup of hot water is placed in the vicinity of the sensor and the RH increases to 80% (right panels). As shown in the macro photograph, the cantilever bends upward, reducing the loading capacitance. As a result, the notch frequency increases to about 2.71 GHz. By connecting the resonator to a broadband antenna, the frequency shift of the resonator can be read wirelessly [25]. Although preliminary, the results demonstrate that paper-based micromachines can be used to implement passive wireless sensors.

D. Wireless Transponders Based on Biopolymers

Research concerning biodegradable and sustainable electronic-based consumer devices is still in its infancy, although recent advances on biodegradable polymers have been reported [98]. Although biodegradability is a key aspect of environmentally friendly sensing devices, sensors

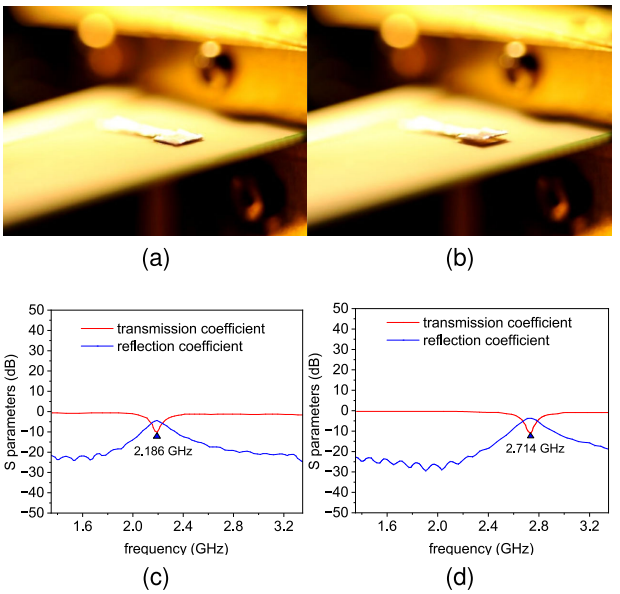

Fig. 32. *Bimorph paper-Al cantilever. (a) and (b) Photographs and (c) and (d) measured scattering parameters for two values of RH: 40% RH [see (a) and (c)] and 80% RH [see (b) and (d)]. As the RH increases, the cantilever bends reducing the filter capacitance. As a consequence, the transmission coefficient peak moves from 2186 to 2714 MHz [25].*

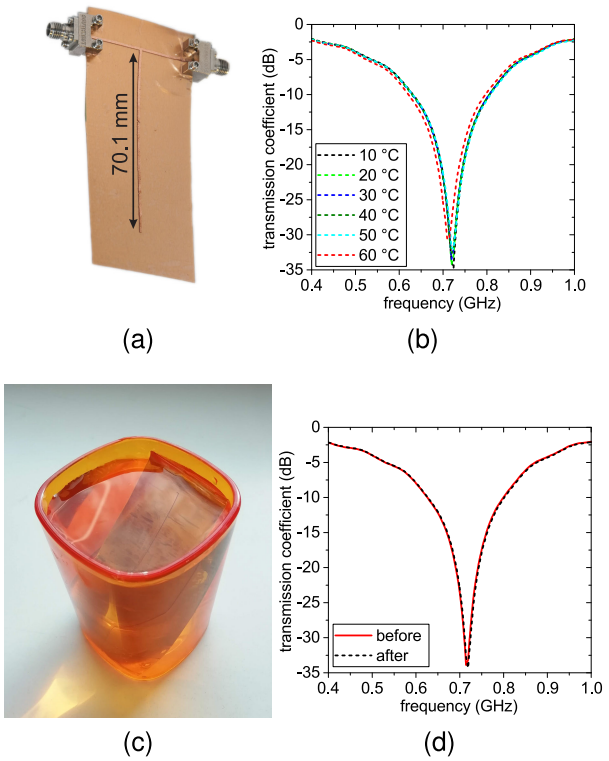

Fig. 33. ***Electromagnetic characterization of PLA versus temperature and water. (a) Photograph of the microstrip T-resonator. (b) Transmission coefficient versus temperature. (c) Resonator immersed in water. (d) Transmission coefficient before and after the immersion. After [101].***

should preserve their sensing feature for a period of time compatible with their life cycle [99].

Bioplastics are particularly appealing for their compostability and low environmental footprint. Based on their manufacturing process, bioplastics can have different mechanical and electromagnetic properties. Although they are not usually able to withstand high temperatures (typical glass transition temperatures of bioplastics such as PLA are around 60 °C [100]), they are generally quite impermeable, which makes them great candidates for outdoor applications.

In [101], an energy-autonomous Radio Frequency IDentification (RFID)-based leaf-temperature sensor was manufactured on a flexible PLA film for smart agriculture applications. The sensor was based on a commercial ultrahigh-frequency (UHF) RFID chip (EM4350B from EM Microelectronic) equipped with an integrated temperature sensor and powered by four flexible solar cells. The antenna of the transponder was manufactured on the PLA substrate with the copper foil technique. The electromagnetic properties of the PLA versus temperature were assessed using a T-resonator with its first resonance in the UHF band [see Fig. 33(a) and (b)]. The material showed stable electromagnetic properties for temperatures up to 50 °C, while only a small downshift of the resonant frequency was observed at the glass transition temperature (in correspondence with the material deformation). In addition, the resonator was first immersed in water for 10 min and then dried at room temperature, as shown in Fig. 33(c), and no variation in the S-parameters was observed [see Fig. 33(d)], demonstrating that the material can be exposed to water without being damaged.

Analogously, a wireless harmonic shock sensor manufactured on a PHBV substrate is illustrated in [102]. PHBV is an interesting substrate material for IoT electronics, due to its low dielectric loss (a loss tangent of 0.008), transparency, and flexibility. PHB, a polyhydroxyalkanoate produced by microorganisms (*Ralstonia euthrophus*, *Bacillus megaterium*, and *Methylbacterium rhodesianum*), is used in tissue engineering because its biodegradation products are nontoxic [103]. The frequency doubler is based on the schematic shown in Fig. 26(c) and it is manufactured with the copper foil technique. The switch is implemented with two copper electrodes separated by a 3-D-printed grid-based regenerated silk (RS), forming a parallel-plate capacitor. The grid features a viscoelastic behavior; if a force above a specific threshold is applied to it, the RS starts to flow under pressure and the two copper electrodes are placed in contact (switch closed). Once the force is removed, the switch returns to the open condition in a certain time period. The prototype shown in Fig. 34(a) works at $f_0 = 2.25$ GHz. The measured RF output power

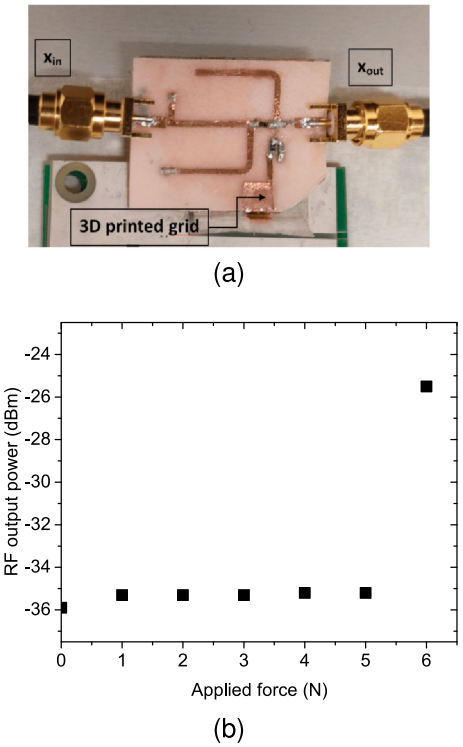

Fig. 34. ***Frequency doubler-based shock sensor on PHBV. (a) Photograph of the prototype and (b) experimental results [102].***

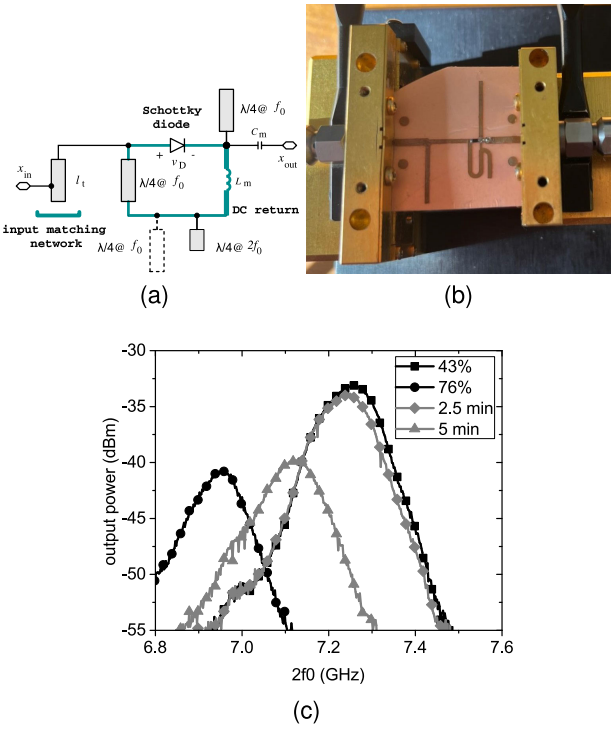

Fig. 35. *Frequency doubler on PHBV. (a) Schematic. (b) Photograph of the prototype. (c) Experimental results.*

at $2f_0$ versus the applied force is shown in Fig. 34(b). The input port of the doubler is connected to a signal generator (an input power of -10 dBm), and the output port is connected to a spectrum analyzer. A variation of about 10 dB in the output power is observed with the switch open and close.

Another frequency doubler prototype on PHBV is shown in Fig. 35(a) and (b). The tag was designed for $f_0 = 3.6$ GHz. The same via-less technique described for the crack sensor is used to avoid vias. In this case, due to the small value of L_m, the quarter-wave open-circuited stub used to create the virtual ground for the f_0 component along the dc return path can be omitted, as this role is played by the quarter-wave open-circuited stub connected at the diode cathode.

It is observed that when the PHBV material is exposed to vapor, a layer of condensation is formed on its surface. Therefore, its optimum operating frequency is down-shifted. If the frequency of the interrogation signal is swept in the frequency range of 3.4–3.6 GHz, the wetness level can be estimated based on the received second harmonic frequency characterized by the lowest conversion loss (i.e., the frequency corresponding to the maximum received power). The results of the experiment are shown in Fig. 35(c). The input power of the frequency doubler is set to -10 dBm. The received power versus frequency is recorded in the laboratory (room temperature and 43% of humidity). The doubler is placed in a sealed box with a hot glass of water and a hygrometer. At equilibrium (a humidity of 76%), the doubler response is recorded (curve labeled as "76%"). Finally, the box is opened, and the doubler response is acquired over time after 2.5 and 5 min. After 5 min, the frequency doubler response is substantially back to its original shape, demonstrating the capability of the adopted materials to work in humid conditions without being damaged.

E. 24-GHz Radar Front End on Paper

Thanks to the high resolution of the copper foil technology (comparable to that of PCBs) and the high conductivity of the obtained metal traces (corresponding to that of the bulk copper), the copper foil technology is suitable to manufacture effective circuits up to millimeter-wave frequencies.

In [75], a continuous-wave radar front end on paper working at 24 GHz is presented. The front end includes the multilayer antenna described in Section III-D, a circular branch-line coupler, and a single-balanced mixer. A commercial oscillator is used to generate the RF transmitted signal (model Hittite HMC739LP4), although a first attempt to manufacture a 24-GHz single-transistor oscillator on paper is presented in [37]. The transmitted RF power is 5 mW.

The radar succeeded in motion sensing in an indoor environment up to a distance of 10 m. Fig. 36(c) shows the measured output signal after amplification associated with a person walking slowly at a speed of 0.4 m/s at a distance of 3 m from the radar.

F. Near-Field Liquid Metal-Based Sensors

Coupled LC tanks can be used to perform near-field contactless sensing in a variety of applications, due to their simplicity and robustness. Based on the information of interest, variations in the mutual coupling or in the resonant frequency of the sensing resonator can be monitored. Such resonators can be manufactured by combining 3-D printing with the afore-described selective-metallization techniques to achieve shapes optimized for the intended application.

In [104], the liquid metal filling technique is used to create an LC tank for motion sensing. The substrate with the microfluidic channels for the spiral coil is 3-D-printed (printer Anycubic Photon M3 Plus, resin Anycubic UV Tough resin). The process, based on SLA, has a resolution of 30 μm on the xy plane and is used to create channels with a diameter of 0.9 mm. The channels are then filled with EGaIn tin. Copper wires are placed in contact with the liquid metal at the two outlets of the spiral. Then, the two apertures are sealed with UV-sensitive resin. Two spirals are manufactured with this technique and are made resonating at 100 kHz. By measuring the variations in the magnitude of the fast Fourier transform of the received signal, both vertical motion and horizontal motion have been detected.

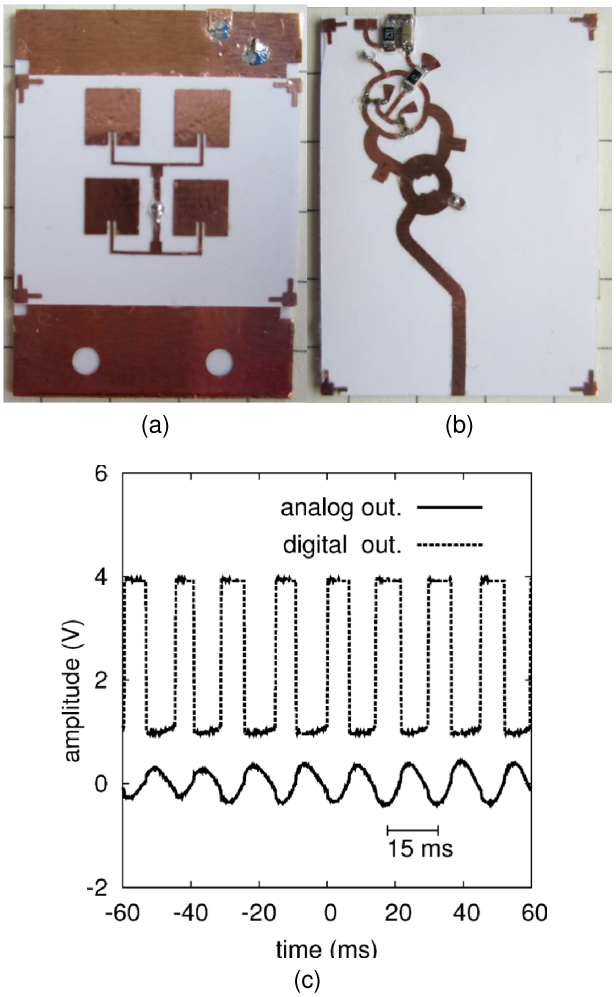

Fig. 36. *24-GHz Doppler radar front end on cellulose. (a) Layout of the top layer, (b) layout of the bottom layer, and (c) output signal associated with a person at a 3-m distance from the radar moving at a speed of 0.4 m/s. The circuit area is 35 × 28 mm. After [76] and [75].*

In [58], an LC tank is embedded in a 3-D-printed cap for food quality monitoring. The circuit includes an inverted-cone-shaped capacitor and a planar-spiral-shaped inductor, which are fit in the cap of a milk package, as shown in Fig. 37(a) and (b). The metal parts are embedded in the 3-D-printed cap by liquid metal filling (a liquid silver suspension is injected in the 3-D-printed channels). By flipping the package, the liquid food to be monitored is trapped inside the capacitor gap. When the liquid deteriorates, its permittivity changes, thereby causing a shift in the resonant frequency of the LC tank. This frequency shift has been monitored wirelessly with a VNA connected to the reader coil coupled to the cap since a change in the permittivity of the trapped liquid causes a frequency shift in the dip of the measured input reflection coefficient. In Fig. 37(c), the cap is placed on a milk package and the resonant frequency of the LC tank is measured over time with the milk correctly stored at 4 °C and with the milk at room temperature. In the first case, the resonant frequency is stable over time, while in the second case, the resonant frequency of the LC tank progressively downshifted.

G. 3-D-Printed Harmonic Pressure Sensor

In [105], the capability of 3-D printing to manufacture 3-D structures that can be compressed or altered mechanically is leveraged to implement wireless pressure sensors. The proposed pressure sensor, whose schematic is shown in Fig. 38, is based on a 2.45-GHz receiving patch antenna, an RF frequency doubler, a pressure transducer based on two coupled quarter-wave microstrip lines, and two 4.9-GHz linearly polarized patch antennas with orthogonal polarization. The applied pressure changes the coupling coefficient between the coupled lines, thereby changing the amount of power transmitted by the antenna connected to the direct port, P_h, with respect to the power transmitted by the antenna connected to the coupled port, P_v.

Fig. 39 shows the layout of the main component of the transponder, i.e., the pressure transducer, which is 3-D directional coupler composed of two coupled microstrip lines facing each other. The microstrip line on Layer2 is connected to Ports 1 and 2 on Layer1 with two parallel-plate waveguides. Since the microstrip on Layer2 is downfaced, while the microstrip line on Layer1 is upfaced, each plate of the parallel-plate waveguides turns into a

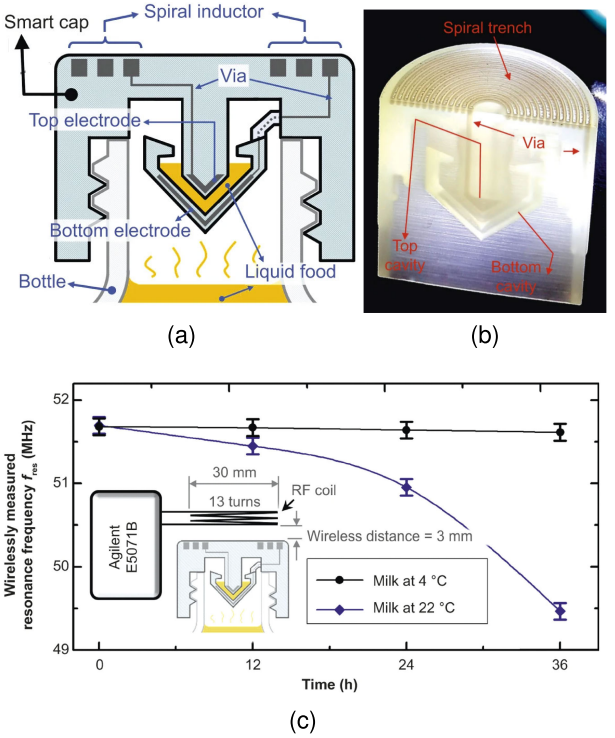

Fig. 37. *Smart cap for food quality monitoring. (a) Schematic of the cap, (b) cross-sectional view, and (c) schematic of the sensing system [58].*

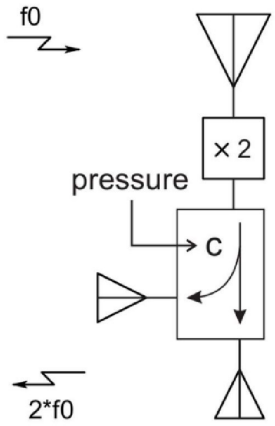

Fig. 38. *Schematic of the 3-D-printed pressure sensor.*

strip at one end and into the ground plane at the other end. This way, the four ports of the component lie on the same layer, so the transducer can be easily connected to the rest of the circuit.

The central frequency of the transducer is $f_0 = 4.9$ GHz. All lines are matched to 50 Ω, including the parallel-plate waveguides that are dimensioned using this equation:

$$Z_0 = \frac{\eta h_p}{w_p} \tag{3}$$

where η is the intrinsic impedance of the substrate, h_p is the distance between the parallel plates, and w_p is the plate width.

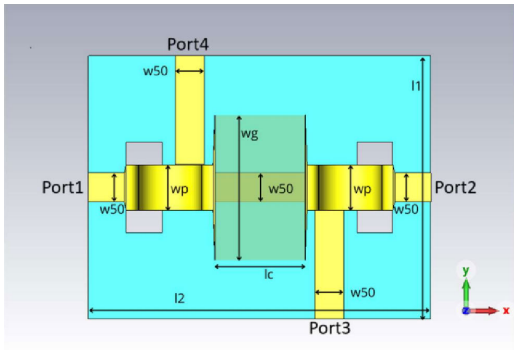

(a)

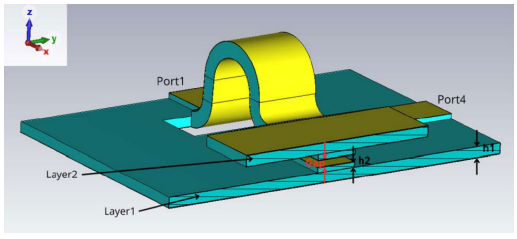

(b)

Fig. 39. *Transducer layout. (a) Top view. (b) Cross section. The main parameters are: $w_{50} = 3.2$ mm, $w_p = 5$ mm, $w_g = 16$ mm, $l_c = 10$ mm, $l_1 = 29$ mm, $l_2 = 38$ mm, $h_1 = 0.8$ mm, $h_2 = 0.4$ mm, and Gap = 0.3–1.5 mm.*

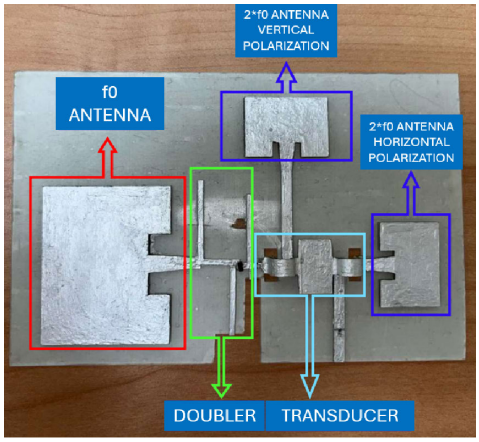

Fig. 40. *3-D-printed pressure sensor. Area: 13.6 × 8.9 cm.*

In Fig. 39, Port 1 is the input port, Port 2 is the transmitting port, Port 3 is the isolated port, and Port 4 is the coupled port. When the pressure is applied on the top layer, the gap between the lines varies, causing an increase in the coupling coefficient between Ports 1 and 4. On the other hand, the transmission coefficient between Ports 1 and Port 2 slightly decreases.

Fig. 40 shows the proof-of-concept prototype manufactured with the embossed-surface patterning technique. The adopted resin is the Clear material from Formlabs. The input port of the pressure transducer is connected to the output port of the frequency doubler. The isolated port is closed on a matched load. Direct and coupled ports are connected to two 4.9-GHz patch antennas with orthogonal

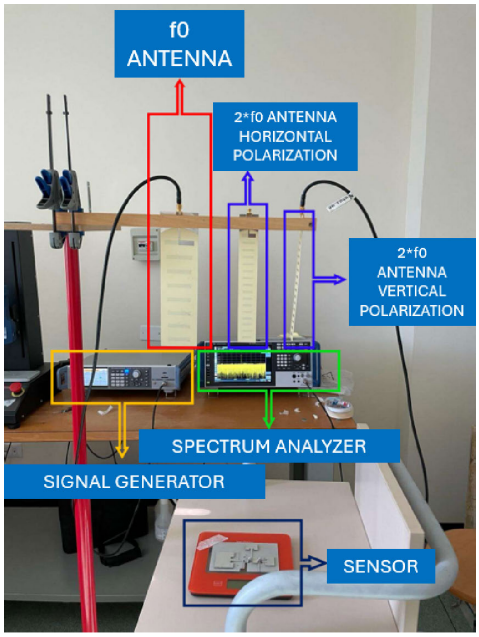

Fig. 41. *Experimental setup for the 3-D-printed pressure sensor.*

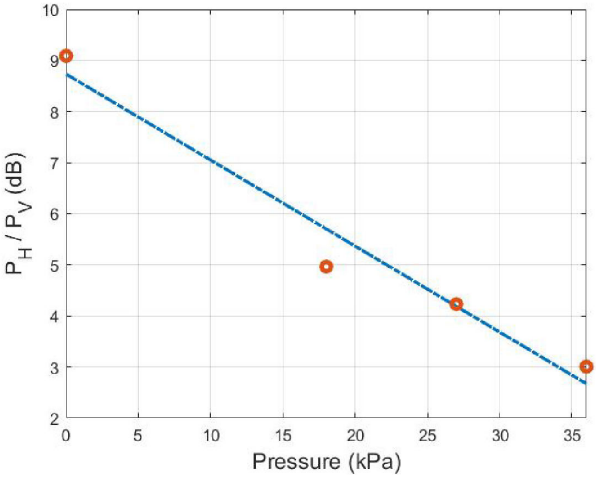

Fig. 42. ***Experimental results for the 3-D-printed pressure sensor: power ratio between the two orthogonal channels. P_V is the power received by the antenna in the vertical polarization, and P_h is the power received by the antenna in the orthogonal polarization.***

polarization. All patch antennas are manufactured following the approach described in Section III-C. To avoid vias between the lines and ground, which would cause manufacturing issues, the board is shaped so that short-circuited stubs and lines extend until the border, where they are folded toward the ground plane.

The reader is equipped with three Yagi–Uda antennas. A photograph of the experimental setup is shown in Fig. 41. The reader is composed of one 2.45-GHz transmitting antenna and two 4.9-GHz receiving antennas with orthogonal polarization. A signal generator is used to feed the 2.45-GHz antenna and the spectrum analyzer is connected alternately to the 4.9-GHz antennas to measure the signal on the direct and coupled port. Pressure is applied on the top of the 3-D directional coupler. The measurement results are shown in Fig. 42. The power ratio varies almost linearly in the considered pressure range (as already noted in [105]), corresponding to an overall variation of about 6 dB for applied pressures up to 35 kPa.

Using an I/Q receiver, the pressure information can be retrieved from the ratio of the power backscattered in the two orthogonal polarizations.

V. CONCLUSION

In this article, we have illustrated some of the emerging room-temperature selective-metallization processes that can be used to manufacture circuits on unconventional and biopolymer materials. The main features of each approach, including copper foil tape, liquid metal, embossed patterning, electroplating, and electroless plating, have been reported, emphasizing their performance in RF applications. Then, some examples of antennas and beamforming networks have been reported, showing the capability of 3-D printing technologies to manufacture innovative and high-performing antenna components in various technologies, including microstrip and coaxial technologies, which can improve the integrability of the sensor node with the hosting object. Finally, additively manufactured wireless transponders based on radar and backscatter radio or near-field communication have been reported and experimentally validated. Although at their infancy, the proposed selective-metallization processes have a good potential for large-area electronics and mass production (for instance, the metal foil tape technique can be compatible with roll-to-roll processes, while the combination of liquid metal and 3-D printing can further enhance the capabilities of microfluidics platforms). In addition, the adoption of innovative low-cost manufacturing technologies, green materials, such as biopolymers and cardboard, and simplified circuit architecture, such as the via-less technique, opens door to the development of a new class of IoT transponders integrated with everyday objects and characterized by a reduced environmental footprint. ■

Acknowledgment

The authors thank Prof. Francesco Cottone from the Department of Physics and Geology, University of Perugia, Perugia, Italy, for his support with 3-D printing prototyping.

REFERENCES

[1] J. M. Williams et al., "Weaving the wireless web: Toward a low-power, dense wireless sensor network for the industrial IoT," *IEEE Microw. Mag.*, vol. 18, no. 7, pp. 40–63, Nov. 2017.
[2] F. A. Almalki et al., "Green IoT for eco-friendly and sustainable smart cities: Future directions and opportunities," *Mobile Netw. Appl.*, vol. 28, no. 1, pp. 178–202, Aug. 2021.
[3] P. Mezzanotte, V. Palazzi, F. Alimenti, and L. Roselli, "Innovative RFID sensors for Internet of Things applications," *IEEE J. Microw.*, vol. 1, no. 1, pp. 55–65, Jan. 2021.
[4] A. Shah, O. Niksan, M. C. Jain, K. Colegrave, M. Wagih, and M. H. Zarifi, "Microwaves see thin ice: A review of ice and snow sensing using microwave techniques," *IEEE Microw. Mag.*, vol. 24, no. 10, pp. 24–39, Oct. 2023.
[5] F. Pereira, R. Correia, P. Pinho, S. I. Lopes, and N. B. Carvalho, "Challenges in resource-constrained IoT devices: Energy and communication as critical success factors for future IoT deployment," *Sensors*, vol. 20, no. 22, p. 6420, Nov. 2020.
[6] L. Portilla et al., "Wirelessly powered large-area electronics for the Internet of Things," *Nature Electron.*, vol. 6, no. 1, pp. 10–17, Dec. 2022.
[7] M. A. Jamshed, K. Ali, Q. H. Abbasi, M. A. Imran, and M. Ur-Rehman, "Challenges, applications, and future of wireless sensors in Internet of Things: A review," *IEEE Sensors J.*, vol. 22, no. 6, pp. 5482–5494, Mar. 2022.
[8] M. J. Tan, C. Owh, P. L. Chee, A. K. K. Kyaw, D. Kai, and X. J. Loh, "Biodegradable electronics: Cornerstone for sustainable electronics and transient applications," *J. Mater. Chem. C*, vol. 4, no. 24, pp. 5531–5558, 2016.
[9] H. Rahmani et al., "Next-generation IoT devices: Sustainable eco-friendly manufacturing, energy harvesting, and wireless connectivity," *IEEE J. Microw.*, vol. 3, no. 1, pp. 237–255, Jan. 2023.
[10] S. K. Behera, "Chipless RFID sensors for wearable applications: A review," *IEEE Sensors J.*, vol. 22, no. 2, pp. 1105–1120, Jan. 2022.
[11] A. Syed Nauroze et al., "Additively manufactured RF components and modules: Toward empowering the birth of cost-efficient dense and ubiquitous IoT implementations," *Proc. IEEE*, vol. 105, no. 4, pp. 702–722, Apr. 2017.
[12] Y. Khan, A. Thielens, S. Muin, J. Ting, C. Baumbauer, and A. C. Arias, "A new frontier of printed electronics: Flexible hybrid electronics," *Adv. Mater.*, vol. 32, no. 15, Nov. 2019, Art. no. 1905279.
[13] M. Ha et al., "Printed, sub-3V digital circuits on plastic from aqueous carbon nanotube inks," *ACS Nano*, vol. 4, no. 8, pp. 4388–4395, Jun. 2010.
[14] W. Smaal et al., "Complementary integrated circuits on plastic foil using inkjet printed n- and p-type organic semiconductors: Fabrication, characterization, and circuit analysis," *Organic Electron.*, vol. 13, no. 9, pp. 1686–1692, Sep. 2012.
[15] M. Kaltenbrunner et al., "An ultra-lightweight design for imperceptible plastic electronics," *Nature*, vol. 499, no. 7459, pp. 458–463, Jul. 2013.

[16] I. J. Fernandes et al., "Silver nanoparticle conductive inks: Synthesis, characterization, and fabrication of inkjet-printed flexible electrodes," *Sci. Rep.*, vol. 10, no. 1, p. 8878, Jun. 2020.

[17] K. Muldoon, Y. Song, Z. Ahmad, X. Chen, and M.-W. Chang, "High precision 3D printing for micro to nano scale biomedical and electronic devices," *Micromachines*, vol. 13, no. 4, p. 642, Apr. 2022.

[18] H. Jeong, Y. Cui, M. M. Tentzeris, and S. Lim, "Hybrid (3D and inkjet) printed electromagnetic pressure sensor using metamaterial absorber," *Additive Manuf.*, vol. 35, Oct. 2020, Art. no. 101405.

[19] E. A. Rojas-Nastrucci et al., "Characterization and modeling of K-band coplanar waveguides digitally manufactured using pulsed picosecond laser machining of thick-film conductive paste," *IEEE Trans. Microw. Theory Techn.*, vol. 65, no. 9, pp. 3180–3187, Sep. 2017.

[20] M. Kacar, T. Weller, and G. Mumcu, "Conductivity improvement of microdispensed microstrip lines and grounded coplanar waveguides using laser micromachining," *IEEE Trans. Compon., Packag. Manuf. Technol.*, vol. 10, no. 12, pp. 2129–2132, Dec. 2020.

[21] C. Crump, V. Gjokaj, B. Wright, J. Papapolymerou, J. D. Albrecht, and P. Chahal, "UV flash sintering of aerosol jet printed silver conductors for microwave circuit applications," *IEEE Trans. Compon., Packag., Manuf. Technol.*, vol. 11, no. 2, pp. 342–350, Feb. 2021.

[22] J. Zhu et al., "Additively manufactured millimeter-wave dual-band single-polarization shared aperture Fresnel zone plate metalens antenna," *IEEE Trans. Antennas Propag.*, vol. 69, no. 10, pp. 6261–6272, Oct. 2021.

[23] M. Li, Y. Yang, Y. Zhang, and F. Iacopi, "3-D printed vertically integrated composite right/left-handed transmission line and its applications to microwave circuits," *IEEE Trans. Microw. Theory Techn.*, vol. 72, no. 6, pp. 3311–3321, Jun. 2024.

[24] J. Zhu and Y. Yang, "3-D printed transmission-reflection-integrated metasurface for spin-decoupled full-space quadruplex channels independent phase modulation," *IEEE Trans. Microw. Theory Techn.*, vol. 72, no. 8, pp. 4790–4800, Aug. 2024.

[25] F. Alimenti et al., "A wireless MEMS humidity sensor based on a paper-aluminium bimorph cantilever," in *IEEE MTT-S Int. Microw. Symp. Dig.*, Jun. 2021, pp. 823–826.

[26] S. A. Nauroze, L. S. Novelino, M. M. Tentzeris, and G. H. Paulino, "Continuous-range tunable multilayer frequency-selective surfaces using origami and inkjet printing," *Proc. Nat. Acad. Sci. USA*, vol. 115, no. 52, pp. 13210–13215, Dec. 2018.

[27] J. Sun and F. Hu, "Three-dimensional printing technologies for terahertz applications: A review," *Int. J. RF Microw. Comput.-Aided Eng.*, vol. 30, no. 1, Oct. 2019, Art. no. e21983.

[28] D. Zhou, X. Huang, and Z. Du, "Analysis and design of multilayered broadband radar absorbing metamaterial using the 3-D printing technology-based method," *IEEE Antennas Wireless Propag. Lett.*, vol. 16, pp. 133–136, 2017.

[29] G.-B. Wu, Y.-S. Zeng, K. F. Chan, S.-W. Qu, J. Shaw, and C. H. Chan, "3-D printed 3-D near-field focus-scanning lens for terahertz applications," *IEEE Trans. Antennas Propag.*, vol. 70, no. 11, pp. 10007–10016, Nov. 2022.

[30] M. Askari et al., "Additive manufacturing of metamaterials: A review," *Additive Manuf.*, vol. 36, Dec. 2020, Art. no. 101562.

[31] J. Fan et al., "A review of additive manufacturing of metamaterials and developing trends," *Mater. Today*, vol. 50, pp. 303–328, Nov. 2021.

[32] K. R. Ryan, M. P. Down, and C. E. Banks, "Future of additive manufacturing: Overview of 4D and 3D printed smart and advanced materials and their applications," *Chem. Eng. J.*, vol. 403, Jan. 2021, Art. no. 126162.

[33] J. K. Gansel et al., "Gold helix photonic metamaterial as broadband circular polarizer," *Science*, vol. 325, no. 5947, pp. 1513–1515, Sep. 2009.

[34] N. Z. Laird et al., "Applications of nanotechnology in 3D printed tissue engineering scaffolds," *Eur. J. Pharmaceutics Biopharmaceutics*, vol. 161, pp. 15–28, Apr. 2021.

[35] F. Alimenti, P. Mezzanotte, M. Dionigi, M. Virili, and L. Roselli, "Microwave circuits in paper substrates exploiting conductive adhesive tapes," *IEEE Microw. Wireless Compon. Lett.*, vol. 22, no. 12, pp. 660–662, Dec. 2012.

[36] V. Palazzi et al., "A novel ultra-lightweight multiband rectenna on paper for RF energy harvesting in the next generation LTE bands," *IEEE Trans. Microw. Theory Techn.*, vol. 66, no. 1, pp. 366–379, Jan. 2018.

[37] V. Palazzi, F. Alimenti, D. Zito, P. Mezzanotte, and L. Roselli, "A 24-GHz single-transistor oscillator on paper," *IEEE Microw. Wireless Compon. Lett.*, vol. 30, no. 11, pp. 1085–1088, Nov. 2020.

[38] C. Mariotti, F. Alimenti, L. Roselli, and M. M. Tentzeris, "High-performance RF devices and components on flexible cellulose substrate by vertically integrated additive manufacturing technologies," *IEEE Trans. Microw. Theory Techn.*, vol. 65, no. 1, pp. 62–71, Jan. 2017.

[39] S. Bittolo Bon et al., "Self-adhesive plasticized regenerated silk on poly(3-hydroxybutyrate-co-3-hydroxyvalerate) for bio-piezoelectric force sensor and microwave circuit design," *J. Appl. Polym. Sci.*, vol. 138, no. 4, p. 49726, Aug. 2020.

[40] M. Degli Esposti, F. Chiellini, F. Bondioli, D. Morselli, and P. Fabbri, "Highly porous PHB-based bioactive scaffolds for bone tissue engineering by in situ synthesis of hydroxyapatite," *Mater. Sci. Eng., C*, vol. 100, pp. 286–296, Jul. 2019.

[41] V. Palazzi et al., "3-D-printing-based selective-ink-deposition technique enabling complex antenna and RF structures for 5G applications up to 6 GHz," *IEEE Trans. Compon., Packag. Manuf. Technol.*, vol. 9, no. 7, pp. 1434–1447, Jul. 2019.

[42] M. Li, Y. Yang, F. Iacopi, J. Nulman, and S. Chappel-Ram, "3D-printed low-profile single-substrate multi-metal layer antennas and array with bandwidth enhancement," *IEEE Access*, vol. 8, pp. 217370–217379, 2020.

[43] A. Vallecchi, D. Cadman, W. G. Whittow, J. Vardaxoglou, E. Shamonina, and C. J. Stevens, "3-D printed bandpass filters with coupled vertically extruded split ring resonators," *IEEE Trans. Microwave Theory Techn.*, vol. 67, no. 11, pp. 4341–4352, Nov. 2019.

[44] E. Márquez-Segura, S.-H. Shin, A. Dawood, N. M. Ridler, and S. Lucyszyn, "Microwave characterization of conductive PLA and its application to a 12 to 18 GHz 3-D printed rotary vane attenuator," *IEEE Access*, vol. 9, pp. 84327–84343, 2021.

[45] Ted Pella Inc. *Pelco®colloidal Silver Product Numbers*. Accessed: Oct. 22, 2024. [Online]. Available: https://www.tedpella.com/technote_html/16031,%2034%20TN.pdf

[46] Formlabs. (Jan. 2019). *Materials Data Sheet Photopolymer Resin for Form 1+ and Form 2*. [Online]. Available: https://archive-media.formlabs.com/upload/XL-DataSheet.pdf

[47] C. Tang, J. Liu, Y. Yang, Y. Liu, S. Jiang, and W. Hao, "Effect of process parameters on mechanical properties of 3D printed PLA lattice structures," *Compos. C, Open Access*, vol. 3, Nov. 2020, Art. no. 100076.

[48] M. Dionigi, C. Tomassoni, G. Venanzoni, and R. Sorrentino, "Simple high-performance metal-plating procedure for stereolithographically 3-D-printed waveguide components," *IEEE Microw. Wireless Compon. Lett.*, vol. 27, no. 11, pp. 953–955, Nov. 2017.

[49] R. Zhang et al., "Effects of DPS on surface roughness and mechanical properties of electrodeposited copper foils," *Crystal Res. Technol.*, vol. 58, no. 10, Aug. 2023, Art. no. 2200260.

[50] S. Ghosh, "Electroless copper deposition: A critical review," *Thin Solid Films*, vol. 669, pp. 641–658, Jan. 2019.

[51] N. Lazarus, J. B. Tyler, J. A. Cardenas, B. Hanrahan, H. Tsang, and S. S. Bedair, "Direct electroless plating of conductive thermoplastics for selective metallization of 3D printed parts," *Additive Manuf.*, vol. 55, Jul. 2022, Art. no. 102793.

[52] M. I. M. Ghazali, S. Karuppuswami, A. Kaur, and P. Chahal, "3-D printed air substrates for the design and fabrication of RF components," *IEEE Trans. Compon., Packag., Manuf. Technol.*, vol. 7, no. 6, pp. 982–989, Jun. 2017.

[53] J. A. Byford, M. I. M. Ghazali, S. Karuppuswami, B. L. Wright, and P. Chahal, "Demonstration of RF and microwave passive circuits through 3-D printing and selective metalization," *IEEE Trans. Compon., Packag., Manuf. Technol.*, vol. 7, no. 3, pp. 463–471, Mar. 2017.

[54] K. Angel, H. H. Tsang, S. S. Bedair, G. L. Smith, and N. Lazarus, "Selective electroplating of 3D printed parts," *Additive Manuf.*, vol. 20, pp. 164–172, Mar. 2018.

[55] S. Akin, C. Nath, and M. B.-G. Jun, "Selective surface metallization of 3D-printed polymers by cold-spray-assisted electroless deposition," *ACS Appl. Electron. Mater.*, vol. 5, no. 9, pp. 5164–5175, Sep. 2023.

[56] H. Wang, A. Enders, J.-A. Preuss, J. Bahnemann, A. Heisterkamp, and M. L. Torres-Mapa, "3D printed microfluidic lab-on-a-chip device for fiber-based dual beam optical manipulation," *Sci. Rep.*, vol. 11, no. 1, p. 14584, Jul. 2021.

[57] W. Su, S. A. Nauroze, B. Ryan, and M. M. Tentzeris, "Novel 3D printed liquid-metal-alloy microfluidics-based zigzag and helical antennas for origami reconfigurable antenna trees," in *IEEE MTT-S Int. Microw. Symp. Dig.*, Jun. 2017, pp. 1579–1582.

[58] S.-Y. Wu, C. Yang, W. Hsu, and L. Lin, "3D-printed microelectronics for integrated circuitry and passive wireless sensors," *Microsyst. Nanoeng.*, vol. 1, no. 1, pp. 1–9, Jul. 2015.

[59] S. Ghosh and S. Lim, "Fluidically switchable metasurface for wide spectrum absorption," *Sci. Rep.*, vol. 8, no. 1, p. 10169, Jul. 2018.

[60] J. Shen, D. P. Parekh, M. D. Dickey, and D. S. Ricketts, "3D printed coaxial transmission line using low loss dielectric and liquid metal conductor," in *IEEE MTT-S Int. Microw. Symp. Dig.*, Jun. 2018, pp. 59–62.

[61] V. Palazzi, A. Cicioni, F. Alimenti, P. Mezzanotte, M. M. Tentzeris, and L. Roselli, "Compact 3-D-printed 4 × 4 Butler matrix based on low-cost and curing-free additive manufacturing," *IEEE Microw. Wireless Compon. Lett.*, vol. 31, no. 2, pp. 125–128, Feb. 2021.

[62] M. D. Dickey, R. C. Chiechi, R. J. Larsen, E. A. Weiss, D. A. Weitz, and G. M. Whitesides, "Eutectic gallium-indium (EGaIn): A liquid metal alloy for the formation of stable structures in microchannels at room temperature," *Adv. Funct. Mater.*, vol. 18, no. 7, pp. 1097–1104, Apr. 2008.

[63] Y. Lin, O. Gordon, M. R. Khan, N. Vasquez, J. Genzer, and M. D. Dickey, "Vacuum filling of complex microchannels with liquid metal," *Lab Chip*, vol. 17, no. 18, pp. 3043–3050, 2017.

[64] M. D. Dickey, "Stretchable and soft electronics using liquid metals," *Adv. Mater.*, vol. 29, no. 27, Apr. 2017, Art. no. 1606425.

[65] V. Palazzi, P. Mezzanotte, F. Alimenti, M. Tentzeris, and L. Roselli, "Microfluidics-based 3D-printed 4 × 4 Butler matrix in coaxial technology for applications up to K band," in *IEEE MTT-S Int. Microw. Symp. Dig.*, Jun. 2019, pp. 1371–1374.

[66] S. Aldrich. *Gallium-Indium Eutectic (495425)*. Accessed: Oct. 22, 2024. [Online]. Available: https://www.sigmaaldrich.com/IT/it/product/aldrich/495425?srsltid=AfmBOor5ZXhcskeQFAa0Dl8DrmlGiZrb4OcJjLca-NfkKMB1XPURCVKC

[67] V. Bharambe, D. P. Parekh, C. Ladd, K. Moussa,

M. D. Dickey, and J. J. Adams, "Vacuum-filling of liquid metals for 3D printed RF antennas," *Additive Manuf.*, vol. 18, pp. 221–227, Dec. 2017.
[68] M. Cosker, L. Lizzi, F. Ferrero, R. Staraj, and J. Ribero, "Realization of 3-D flexible antennas using liquid metal and additive printing technologies," *IEEE Antennas Wireless Propag. Lett.*, vol. 16, pp. 971–974, 2017.
[69] Y.-W. Wu, S. Alkaraki, S.-Y. Tang, Y. Wang, and J. R. Kelly, "Circuits and antennas incorporating gallium-based liquid metal," *Proc. IEEE*, vol. 111, no. 8, pp. 955–977, Aug. 2023.
[70] J. Ma et al., "Metallophobic coatings to enable shape reconfigurable liquid metal inside 3D printed plastics," *ACS Appl. Mater. Interface*, vol. 13, no. 11, pp. 12709–12718, Nov. 2020.
[71] H. Ren, B. Arigong, M. Zhou, J. Ding, and H. Zhang, "A novel design of 4 × 4 Butler matrix with relatively flexible phase differences," *IEEE Antennas Wireless Propag. Lett.*, vol. 15, pp. 1277–1280, 2016.
[72] S. Kim, S. Yoon, Y. Lee, and H. Shin, "A miniaturized Butler matrix based switched beamforming antenna system in a two-layer hybrid stackup substrate for 5G applications," *Electronics*, vol. 8, no. 11, p. 1232, Oct. 2019.
[73] S. Trinh-Van, J. M. Lee, Y. Yang, K.-Y. Lee, and K. C. Hwang, "A sidelobe-reduced, four-beam array antenna fed by a modified 4 × 4 Butler matrix for 5G applications," *IEEE Trans. Antennas Propag.*, vol. 67, no. 7, pp. 4528–4536, Jul. 2019.
[74] V. Palazzi, F. Alimenti, C. Kalialakis, P. Mezzanotte, A. Georgiadis, and L. Roselli, "Highly integrable paper-based harmonic transponder for low-power and long-range IoT applications," *IEEE Antennas Wireless Propag. Lett.*, vol. 16, pp. 3196–3199, 2017.
[75] F. Alimenti et al., "A 24-GHz front-end integrated on a multilayer cellulose-based substrate for Doppler radar sensors," *Sensors*, vol. 17, no. 9, p. 2090, Sep. 2017.
[76] F. Alimenti et al., "24-GHz CW radar front-ends on cellulose-based substrates: A new technology for low-cost applications," in *IEEE MTT-S Int. Microw. Symp. Dig.*, May 2015, pp. 1–4.
[77] L. Balocchi, V. Palazzi, S. Bonafoni, F. Alimenti, P. Mezzanotte, and L. Roselli, "Compact green harmonic transponders for parcel tracking," *IEEE J. Radio Freq. Identificat.*, vol. 7, pp. 247–256, 2023.
[78] X. Gu, N. N. Srinaga, L. Guo, S. Hemour, and K. Wu, "Diplexer-based fully passive harmonic transponder for sub-6-GHz 5G-compatible IoT applications," *IEEE Trans. Microw. Theory Techn.*, vol. 67, no. 5, pp. 1675–1687, May 2019.
[79] M. Virili et al., "7.5–15 MHz organic frequency doubler made with pentacene-based diode and paper substrate," in *IEEE MTT-S Int. Microw. Symp. Dig.*, Jun. 2014, pp. 1–4.
[80] K. Gallagher, R. Narayanan, G. Mazzaro, A. Martone, and K. Sherbondy, "Static and moving target imaging using harmonic radar," *Electronics*, vol. 6, no. 2, p. 30, Apr. 2017.
[81] F. Zhu, K. Wang, and K. Wu, "A fundamental-and-harmonic dual-frequency Doppler radar system for vital signs detection enabling radar movement self-cancellation," *IEEE Trans. Microw. Theory Techn.*, vol. 66, no. 11, pp. 5106–5118, Nov. 2018.
[82] *The RECCO System*. Accessed: Oct. 22, 2024. [Online]. Available: https://recco.com/technology/
[83] B. G. Colpitts and G. Boiteau, "Harmonic radar transceiver design: Miniature tags for insect tracking," *IEEE Trans. Antennas Propag.*, vol. 52, no. 11, pp. 2825–2832, Nov. 2004.
[84] S. Lioy et al., "Tracking the invasive hornet *Vespa velutina* in complex environments by means of a harmonic radar," *Sci. Rep.*, vol. 11, no. 1, p. 12143, Jun. 2021.
[85] V. Palazzi, L. Roselli, M. M. Tentzeris, P. Mezzanotte, and F. Alimenti, "Energy-efficient harmonic transponder based on on-off keying modulation for both identification and sensing," *Sensors*, vol. 22, no. 2, p. 620, Jan. 2022.
[86] V. Palazzi, F. Alimenti, P. Mezzanotte, M. M. Tentzeris, and L. Roselli, "Passive wireless vibration sensors based on the amplitude modulation of harmonic backscattering," *IEEE Trans. Microw. Theory Techn.*, vol. 72, no. 6, pp. 3841–3853, Jun. 2024.
[87] M. I. M. Ghazali, S. Karuppuswami, and P. Chahal, "3-D printed embedded passive harmonic sensor tag as markers for buried assets localization," *IEEE Sens. Lett.*, vol. 3, no. 4, pp. 1–4, Apr. 2019.
[88] V. Palazzi, F. Alimenti, P. Mezzanotte, G. Orecchini, and L. Roselli, "Zero-power, long-range, ultra low-cost harmonic wireless sensors for massively distributed monitoring of cracked walls," in *IEEE MTT-S Int. Microw. Symp. Dig.*, Jun. 2017, pp. 1335–1338.
[89] S.-Y. Cho, J.-G. Kim, and C.-M. Chung, "A fluorescent crack sensor based on cyclobutane-containing crosslinked polymers of tricinnamates," *Sens. Actuators B, Chem.*, vol. 134, no. 2, pp. 822–825, Sep. 2008.
[90] X. Yi, J. Cooper, Y. Wang, M. Tentzeris, and R. Leon, "Wireless crack sensing using an RFID-based folded patch antenna," in *Proc. 6th Int. Conf. Bridge Maintenance, Saf. Manag. (IABMAS)*, 2012, pp. 1–7.
[91] P. Kalansuriya, R. Bhattacharyya, and S. Sarma, "RFID tag antenna-based sensing for pervasive surface crack detection," *IEEE Sensors J.*, vol. 13, no. 5, pp. 1564–1570, May 2013.
[92] C. Cho, X. Yi, D. Li, Y. Wang, and M. M. Tentzeris, "Passive wireless frequency doubling antenna sensor for strain and crack sensing," *IEEE Sensors J.*, vol. 16, no. 14, pp. 5725–5733, Jul. 2016.
[93] S. Caizzone, E. DiGiampaolo, and G. Marrocco, "Wireless crack monitoring by stationary phase measurements from coupled RFID tags," *IEEE Trans. Antennas Propag.*, vol. 62, no. 12, pp. 6412–6419, Dec. 2014.
[94] J. Zhang, B. Huang, G. Zhang, and G. Tian, "Wireless passive ultra high frequency RFID antenna sensor for surface crack monitoring and quantitative analysis," *Sensors*, vol. 18, no. 7, p. 2130, Jul. 2018.
[95] S. Dey, P. Kalansuriya, and N. C. Karmakar, "Novel chipless RFID high resolution crack sensor based on SWB technology," *IEEE Sensors J.*, vol. 21, no. 3, pp. 2908–2920, Feb. 2021.
[96] N. Javed, M. A. Azam, and Y. Amin, "Chipless RFID multisensor for temperature sensing and crack monitoring in an IoT environment," *IEEE Sensors Lett.*, vol. 5, no. 6, pp. 1–4, Jun. 2021, Art. no. 6001404.
[97] J. Bito et al., "Millimeter-wave ink-jet printed RF energy harvester for next generation flexible electronics," in *Proc. IEEE Wireless Power Transf. Conf. (WPTC)*, May 2017, pp. 1–4.
[98] M. Irimia-Vladu, "Green electronics: Biodegradable and biocompatible materials and devices for sustainable future," *Chem. Soc. Rev.*, vol. 43, no. 2, pp. 588–610, 2014.
[99] A. A. Shah, F. Hasan, A. Hameed, and S. Ahmed, "Biological degradation of plastics: A comprehensive review," *Biotechnol. Adv.*, vol. 26, no. 3, pp. 246–265, May 2008.
[100] A. Södergård and M. Stolt, "Properties of lactic acid based polymers and their correlation with composition," *Prog. Polym. Sci.*, vol. 27, no. 6, pp. 1123–1163, Jul. 2002.
[101] V. Palazzi, S. Bonafoni, F. Alimenti, P. Mezzanotte, and L. Roselli, "Feeding the world with microwaves: How remote and wireless sensing can help precision agriculture," *IEEE Microw. Mag.*, vol. 20, no. 12, pp. 72–86, Dec. 2019.
[102] M. R. Ceccarini et al., "Biomaterial inks from peptide-functionalized silk fibers for 3D printing of futuristic wound-healing and sensing materials," *Int. J. Mol. Sci.*, vol. 24, no. 2, p. 947, Jan. 2023.
[103] P. L. B. Araujo, C. R. P. C. Ferreira, and E. S. Araujo, "Biodegradable conductive composites of poly(3-hydroxybutyrate) and polyaniline nanofibers: Preparation, characterization and radiolytic effects," *Exp. Polym. Lett.*, vol. 5, no. 1, pp. 12–22, 2011.
[104] R. Chirila, A. S. Dahiya, C. Urlea, P. Schyns, and R. Dahiya, "3-D printed microfluidic coils with liquid metal for wireless motion sensing," *IEEE Sensors Lett.*, vol. 7, no. 6, pp. 1–4, Jun. 2023.
[105] V. Palazzi, M. Tentzeris, F. Alimenti, P. Mezzanotte, and L. Roselli, "A novel additively-manufactured pressure transducer for zero-power wireless sensing," in *Proc. 52nd Eur. Microw. Conf. (EuMC)*, Sep. 2022, pp. 68–71.

ABOUT THE AUTHORS

Valentina Palazzi (Senior Member, IEEE) received the M.S. degree in electrical engineering and the Ph.D. degree in industrial and information engineering from the University of Perugia, Perugia, Italy, in 2014 and 2018, respectively.

She was a Visiting Ph.D. Student with the Tyndall National Institute, Cork, Ireland, in summer of 2015. In 2016, she did a short-term scientific mission with the Centre Tecnològic de Telecomunicacions de Catalunya, Barcelona, Spain, sponsored by the cost action IC1301 "WiPE." From December 2016 to April 2017, she was a Student Intern with the Agile Technologies for High-Performance Electromagnetic Novel Applications Research Group, School of Electrical and Computer Engineering, Georgia Institute of Technology, Atlanta, GA, USA. Since 2019, she has been a Researcher with the High Frequency Electronics Laboratory, Department of Engineering, University of Perugia. She has co-authored more than 80 articles and holds three patents. Her current research interests include wireless sensors, radar front ends, wireless power transfer technologies, beamforming networks, additive manufacturing processes, and conformal electronics.

Dr. Palazzi was an Elected Voting Member of the IEEE Microwave Theory and Technology Society (MTT-S) Administrative Committee from 2024 to 2026. She is a member of IEEE MTT-S Technical Committees 16 "Microwave and Millimeter Wave Packaging Interconnect and Integration," 17 "Microwave Materials and Processing Technologies," and 26 "RFID, Wireless Sensor and IoT." She was the Chair of the TC 26 from 2022 to 2023. She was an Early Career Representative of the URSI Commission D "Electronics and Photonics" of the International Union of Radio Science (URSI) from 2021 to 2026. She was a recipient of the First Place Award of the Student Design Competition on Wireless Energy Harvesting at the 2016 IEEE MTT-S International Microwave Symposium (IMS), the IEEE MTT-S Graduate Fellowship in 2017, the 2017 MTT-S Prize–Italy Chapter Central and Southern Italy, the URSI Young Scientist Best

Paper Award conferred at the 2019 URSI Italian National Meeting, the Second Place at the 3 Minute Thesis Competition at IMS 2021, and the GAAS Young Scientist Recognition (URSI Commission D) conferred at General Assembly and Scientific Symposium (GASS) 2021. Since 2025, she has served as an Associate Editor for *IEEE Microwave and Technology Letters*.

Federico Alimenti (Senior Member, IEEE) received the Laurea degree (magna cum laude) and the Ph.D. degree in electronic engineering from the University of Perugia, Perugia, Italy, in 1993 and 1997, respectively. In 1993, he completed an internship at Daimler-Benz Aerospace, Ulm, Germany.

He was a Visiting Scientist at the Technical University of Munich, Munich, Germany. In summer 2014, he was a Visiting Professor at the École Polytechnique Fédérale de Lausanne (EPFL), Lausanne, Switzerland. He is currently an Associate Professor of electronics at the University of Perugia. In 2001, he was awarded a research fellowship at the Department of Electronic and Information Engineering, University of Perugia. From 2006 to 2010, he was an elected member of the Academic Senate of the University of Perugia. From 2011 to 2014, he was a Scientific Coordinator of the ARTEMOS project, ENIAC Call 3, 2010. From 2019 to 2022, he coordinated an industrial research project on integrated noise built-in test equipment for millimeter-wave receiver calibration, funded by Infineon Technologies Austria. In the last years, he coordinated several national research projects (e.g., PRIN-2017 ENTERPRISING and PRIN-2022 SIPT-VARIS) and collaborated with Picosats s.r.l., Trieste, Italy, to develop Ku- and Ka-band radio transceivers for Cubesat applications. In 2023, these transceivers received the flight heritage and worked correctly for about a year on an LEO platform. He has authored more than 220 papers in refereed journals and conference proceedings. He has co-authored book chapters and holds several patents. His H-index is 27 with more than 2800 citations (source Scopus). His scientific interests include the design and experimental characterization of radio frequency (RF) integrated circuits in CMOS and SiGe BiCMOS technologies, the modeling and design of integrated avalanche noise sources for millimeter-wave applications, and the development of microwave systems and scientific instruments for space applications.

Dr. Alimenti received the URSI Young Scientist Award in 1996 and the IET Premium (Best Paper) Award in 2013. He received the Best Conference Paper Award at IEEE RFID Technology and Applications Conference, Tampere, Finland, in September 2014. He was a co-recipient of the Best Student Paper Award at IEEE Wireless Power Transfer Conference, Jeju, South Korea, in May 2014. In 2018, he obtained the qualification of Full Professor and won the Mario Sannino Award for the best research in the field of microwave electronics. In 2012, he won the Element 14 Medical Design Award by proposing a disposable clinical thermometer on a band-aid. He was the Technical Program Committee (TPC) Chair of the IEEE Wireless Power Transfer (WPT) Conference. In 2017, he participated as a keynote lecturer in the summer school held at Infineon Austria AG, Villach.

Leonardo Pierantozzi received the M.S. degree (magna cum laude) in electrical engineering from the University of Perugia, Perugia, Italy, in 2022.

His research interests include additive manufacturing for sensing and reconfigurable radio frequency (RF) components.

Matteo Ribeca received the B.S. degree in electrical engineering from the University of Perugia, Perugia, Italy, in 2021.

His research interests include additive manufacturing and passive components for beamforming networks.

Leonardo Balocchi (Student Member, IEEE) received the M.S. degree (magna cum laude) in electrical engineering from the University of Perugia, Perugia, Italy, in 2021.

His research interests include distributed sensing and Radio Frequency IDentification (RFID) transponders.

Luca Valentini received the master's degree in physics from the University of Perugia, Perugia, Italy, in 1997, and the Ph.D. degree in materials science from the University of Naples "Federico II," Naples, Italy, in 2001.

From 2006 to 2015, he was an Assistant Professor at the University of Perugia. He is currently an Associate Professor of materials science and technology at the Civil and Environmental Engineering Department, University of Perugia, and the INSTM Research Unit, Florence, Italy. He has more than 190 publications in international journals with a citation index of 43 in the fields of nanomaterials, polymer science, and nanodevices.

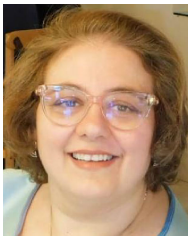

Silvia Bittolo Bon received the master's degree in materials engineering and the Ph.D. degree in materials nanotechnology from the University of Perugia, Perugia, Italy, in 2003 and 2008, respectively.

She has been working at the Civil and Environmental Engineering Department, University of Perugia, since 2008. She is the author of more than 60 publications in international journals in the fields of materials science and polymer science. She is involved in research activities in the field of the development and characterization of nanostructured multifunctional hybrid materials and bionic composites.

Paolo Mezzanotte (Member, IEEE) was born in Perugia, Italy, in 1965. He received the Ph.D. degree from the University of Perugia, Perugia, in 1997.

Since 2007, he has been an Associate Professor with the University of Perugia, where he has been involved in teaching the classes "Radio Frequencies Engineering" and "Systems and Circuits for IoT." He was the Vice Head of the Department of Engineering, University of Perugia, from 2014 to 2019. His present H-index is 34 (source Scopus). His current research interests include the development of microwave circuits on biocompatible substrates and the enabling technologies for the Internet of Things (IoT). These research activities are testified by over 170 publications in the most reputed specialized journals and at the main conferences of the microwave scientific community.

Dr. Mezzanotte served as the Chair for the IEEE Technical Committee MTT-24-RFID Technologies from 2018 to 2019. He is the Chair of the IEEE Topical Conference on Wireless Sensors and Sensor Networks (WiSNet). He is also an Associate Editor of *Applied Computational Electromagnetics Society Journal* and IEEE Journal of Microwaves.

Manos M. Tentzeris (Fellow, IEEE) received the Diploma degree (magna cum laude) in electrical and computer engineering from the National Technical University of Athens, Athens, Greece, in 1992, and the M.S. and Ph.D. degrees in electrical engineering and computer science from the University of Michigan, Ann Arbor, MI, USA, in 1994 and 1998, respectively.

He was a Visiting Professor with the Technical University of Munich, Munich, Germany, in 2002; GTRI-Ireland, Athlone, Ireland, in 2009; and LAAS-CNRS, Toulouse, France, in 2010. He was a Humboldt Guest Professor with FAU, Nuremberg, Germany, in 2019. He is currently the Ed and Pat Joy Chair Professor with the School of Electrical and Computer Engineering, Georgia Institute of Technology, Atlanta, GA, USA, where he heads the ATHENA Research Group. He was the Head of the GT ECE Electromagnetics Technical Interest Group; the Associate Director of Radio Frequency IDentification (RFID)/Sensors research, Georgia Electronic Design Center; the Associate Director of RF, Research Georgia Institute of Technology NSF-Packaging Research Center; and the RF Alliance Leader. He has helped develop academic programs in 3-D/inkjet-printed radio frequency (RF) electronics and modules, flexible electronics, origami and morphing electromagnetics, highly integrated/multilayer packaging for RF, millimeter-wave, sub-terahertz (THz), and wireless applications using ceramic and organic flexible materials, 5G/6G/sub-THz interconnects, packaging and modules, 4-D RF electronics and phased arrays, paper-based RFIDs and sensors, wireless sensors and biosensors, wearable electronics, "Green" and transient electronics, energy harvesting and wireless power transfer, nanotechnology applications in RF, microwave micro-electromechanical system (MEMS), and system on package (SOP)-integrated (UWB, multiband, millimeter wave (mmW), and conformal) antennas. He has authored more than 850 papers in refereed journals and conference proceedings, seven books, and 26 book chapters.

Dr. Tentzeris is a member of the URSI-Commission D, the MTT-15 Committee, and the Technical Chamber of Greece; an Associate Member of European Mcirowave Association (EuMA); and a Fellow of the Electromagnetic Academy. He was a recipient/co-recipient of the 2022 Georgia Tech Outstanding Doctoral Thesis Advisor Award, the 2021 IEEE Antennas and Propagation Symposium (APS) Best Student Paper Award, the 2019 Humboldt Research Prize, the 2017 Georgia Institute of Technology Outstanding Achievement in Research Program Development Award, the 2016 Bell Labs Award Competition 3rd Prize, the 2015 IET Microwaves, Antennas, and Propagation Premium Award, the 2014 Georgia Institute of Technology ECE Distinguished Faculty Achievement Award, the 2014 IEEE RFID-TA Best Student Paper Award, the 2013 IET Microwaves, Antennas and Propagation Premium Award, the 2012 FiDiPro Award in Finland, the iCMG Architecture Award of Excellence, the 2010 IEEE Antennas and Propagation Society Piergiorgio L. E. Uslenghi Letters Prize Paper Award, the 2011 International Workshop on Structural Health Monitoring Best Student Paper Award, the 2010 Georgia Institute of Technology Senior Faculty Outstanding Undergraduate Research Mentor Award, the 2009 IEEE Transactions on Components and Packaging Technologies Best Paper Award, the 2009 E. T. S. Walton Award from the Irish Science Foundation, the 2007 IEEE AP-S Symposium Best Student Paper Award, the 2007 IEEE MTT-S IMS Third Best Student Paper Award, the 2007 ISAP 2007 Poster Presentation Award, the 2006 IEEE MTT-S Outstanding Young Engineer Award, the 2006 Asia–Pacific Microwave Conference Award, the 2004 IEEE Transactions on Advanced Packaging Commendable Paper Award, the 2003 NASA Godfrey "Art" Anzic Collaborative Distinguished Publication Award, the 2003 IBC International Educator of the Year Award, the 2003 IEEE CPMT Outstanding Young Engineer Award, the 2002 International Conference on Microwave and Millimeter-Wave Technology Best Paper Award (Beijing, China), the 2002 Georgia Institute of Technology–ECE Outstanding Junior Faculty Award, the 2001 ACES Conference Best Paper Award, the 2000 NSF CAREER Award, and the 1997 Best Paper Award of the International Hybrid Microelectronics and Packaging Society. He was the General Co-Chair of the 2023 IEEE Wireless Power Transfer Technology Conference and Expo (WPTCE) in San Diego and the 2019 IEEE APS Symposium in Atlanta. He was the TPC Chair of the IEEE MTT-S IMS 2008 Symposium and the Chair of the 2005 IEEE CEM-TD Workshop. He is the Vice-Chair of the RF Technical Committee (TC16) of the IEEE CPMT Society. He is the Founder and the Chair of the RFID Technical Committee (TC24) of the IEEE MTT-S and the Secretary/Treasurer of the IEEE C-RFID. He has served as an Associate Editor for IEEE TRANSACTIONS ON MICROWAVE THEORY AND TECHNIQUES, IEEE TRANSACTIONS ON ADVANCED PACKAGING, and *International Journal on Antennas and Propagation*. He has given more than 150 invited talks to various universities and companies all over the world. He is currently one IEEE EPS Distinguished Lecturer and he has served as one of the IEEE MTT-S Distinguished Microwave Lecturers and one of the IEEE CRFID Distinguished Lecturers.

Luca Roselli (Fellow, IEEE) joined the University of Perugia, Perugia, Italy, in 1991. In 2000, he founded the spin-off WiS Srl, Foligno, Italy. He was involved in electronic technologies for the Internet of Things for six years. He was a member of the Board of Directors of ART S.r.l., Urbino, Italy, from 2008 to 2012. He is currently a Full Professor with the University of Perugia, where he teaches applied electronics and coordinates the High Frequency Electronics Laboratory. He has authored over 280 papers (H index of 41 and i10 of 120, over 5000 citations—Scholar) and *Green RFID System* (Cambridge Univ. Press, 2014). His current research interests include HF electronic systems with special attention to Radio Frequency IDentification (RFID), new materials, and wireless power transfer.

Dr. Roselli is a member of the list of experts of Italian Ministry of Research; the past Chair of the IEEE Technical Committees MTT-24-RFID; the Vice Chair of 25-RF Nanotechnologies, 26-Wireless Power Transfer, the ERC Panel PE7, and the Advisory Committee of the IEEE-WPTC; and the Chair of the SC-32 of IMS. He is the Co-Chair of the IEEE Wireless Sensor Network Conference. He organized the VII Computational Electromagnetic Time Domain in 2007 and the first IEEE Wireless Power Transfer Conference in 2013. He is an Associate Editor of *IEEE Microwave Magazine*. He is involved on the boards of several international conferences. He is a reviewer for many international reviews, including PROCEEDINGS OF THE IEEE, IEEE TRANSACTIONS ON MICROWAVE THEORY AND TECHNIQUES, and IEEE MICROWAVE AND WIRELESS COMPONENTS LETTERS.

Open Access funding provided by 'Università degli Studi di Perugia' within the CRUI CARE Agreement